Exploring UE Sensing Capabilities for Integrated Sensing and Communication

POORIYA SAMADIFAR & ANVEEKSHA KURAPATI
MASTER´S THESIS
DEPARTMENT OF ELECTRICAL AND INFORMATION TECHNOLOGY
FACULTY OF ENGINEERING | LTH | LUND UNIVERSITY

LUND UNIVERSITY

ERICSSON

Exploring UE Sensing Capabilities for Integrated Sensing and Communication

Pooriya Samadifar, Anveeksha Kurapati
po2404sa-s@student.lu.se, an3874ku-s@student.lu.se

Department of Electrical and Information Technology
Lund University

Supervisors: Juan Vidal Alegria
Company supervisor: Magnus Jönsson.L

Examiner: Ove Edfors

June 10, 2024

Printed in Sweden
Tryckeriet i E-huset, Lund

Abstract

In the realm of wireless communications, the exploration of user equipment (UE) sensing capabilities has emerged as a complementary approach for optimizing the performance of wireless networks. This thesis delves into the potential enhancements achievable by integrating UE sensing capabilities into wireless networks, focusing on detecting Line Of Sight (LOS) and Non Line Of Sight (NLOS) scenarios. While traditional beamforming algorithms have played a pivotal role in network optimization, this research aims to broaden the scope by investigating how UE sensing can complement existing techniques. By harnessing real-time UE sensing data, encompassing channel conditions and interference levels, adaptive adjustments in network parameters can be made to enhance throughput, coverage, and energy efficiency. The effectiveness and use cases of incorporating LOS/NLOS detection using deep-learning models into network optimization strategies are demonstrated through simulation-based evaluations. Notably, the simulations provide valuable insights into the impact of UE direction movement towards or away from the base station (BS), UE arrival time to the LOS region, and the size of the obstacle obstructing the communication between the BS and UE. These findings contribute to the body of knowledge in the field and shed light on the potential of UE sensing in optimizing wireless network performance.

Acknowledgements

We sincerely thank Dr. Juan Vidal Alegria, our supervisor at Lund University, for his invaluable guidance and support throughout our master's thesis journey. We also express our heartfelt appreciation to Magnus Jönsson L, our supervisor at Ericsson, for his valuable insights and unwavering support. Furthermore, we acknowledge the professors at Lund University for their dedication to teaching and mentorship, and our colleagues at Ericsson for their collaboration and contributions. We are grateful for the collective support and guidance that has shaped our academic and professional growth.

Anveeksha Kurapati and Pooriya Samadifar

I want to express my deepest gratitude to my wife, Nazanin, whose unwavering support and belief in me have been the bedrock of my journey. Her constant encouragement and faith in my abilities have been a source of strength and inspiration throughout the program.
To my family, who, despite the physical distance, have provided an immeasurable amount of emotional support. Their love and belief in my endeavors have been a guiding light, reminding me of the warmth and comfort of home even from afar.

Pooriya Samadifar

I am immensely grateful to my beloved family - my husband, Sandeep, and our children, Joshika and Ketan - for their unwavering love and support throughout my academic journey. I feel truly blessed to have them by my side.
My heartfelt gratitude extends to my parents and in-laws, whose steadfast belief, valuable guidance, and continuous encouragement have been instrumental in my success. I am deeply thankful to my dear friends and well-wishers, who have been a source of strength and inspiration, offering encouragement and genuine care.

Anveeksha Kurapati

Popular Science Summary

The Fifth Generation (5G) technology heralds a significant revolution in wireless communication, characterized by notable advancements in data rates, latency, connectivity, and reliability. Through its ability to deliver substantially higher data rates and ultra-low latency, 5G facilitates rapid access to large data files and immersive multimedia experiences. The technology's capacity for massive connectivity, achieved through techniques like massive MIMO which means very large number of antennas at the Base Station (BS) with many users, unlocks the potential for extensive implementation of the Internet of Things (IoT). IoT refers to devices equipped with sensors, processing capabilities, software, and other technologies, enabling them to connect and share data with other devices and systems via the Internet or other communication networks. Additionally, 5G's enhanced reliability and expanded coverage ensure consistent connectivity, even in challenging environments. The far-reaching applications of 5G encompass various sectors, fostering innovation in areas such as smart cities, healthcare, transportation, and industrial automation. This transformative technology empowers emerging fields like autonomous vehicles, telemedicine, smart grids, and precision agriculture, reshaping industries and revolutionizing societal interactions.

Imagine a world where your smartphone not only connects you to the internet but also helps monitor your surroundings. This vision is becoming a reality with the advancement of 5G technology. In particular, researchers are exploring the potential of integrating sensing capabilities into 5G communication networks. This means that the same infrastructure that enables your phone, calls, and internet browsing, can also be used for tasks like environmental monitoring or healthcare applications. One promising approach involves utilizing a signal called Uplink Sounding Reference Signal (ULSRS), which is already used in 5G networks for communication and sensing purposes. By cleverly analyzing this signal, researchers can gather valuable information about the surrounding environment or specific phenomena. This integration of sensing and communication opens up exciting possibilities for a wide range of applications, making our world smarter and more connected than ever before.

Table of Contents

List of Figures

List of Tables

List of Abbreviations & Acronyms

3GPP	3rd Generation Partnership Project
5G	Fifth Generation
ANN	Artificial Neural Network
AoA	Angle of Arrival
AoD	Angle of Departure
AS	Angle Spread
BS	Base Station
CAP	Convolutional Activation Pooling
CIR	Channel Impulse Response
CNN	Convolutional Neural Network
CP	Cyclic Prefix
CSI	Channel State Information
CSI-RS	CSI Reference Signals
DL	Downlink
DNN	Deep Neural Network
DS	Delay Spread
FFT	Fast Fourier Transform
FR1	Frequency range 1
FR2	Frequency range 2

GCS	Geographic Coordinate System
IoT	Internet of Things
ISI	Inter Symbol Interference
LOS	Line Of Sight
LSP	Large Scale Parameters
LTE	Long Term Evolution
MIMO	Multiple Input Multiple Output
ML	Machine Learning
MPC	Multipath Components
MS	Mobile Station
MU-MIMO	Multi-user Multiple Input Multiple Output
NLOS	Non Line Of Sight
NR	New Radio
OFDM	Orthogonal Frequency Division Multiplexing
PDP	Power Delay Profile
PL	Path-loss
PRBs	Physical Resource Blocks
PRS	Positioning Reference Signal
RAT	Radio Access Technology
RB	Resource Block
ReLU	Rectified Linear Unit
SCS	Subcarrier Spacing
SD	Standard Deviation
SF	Shadow Fading
SIMO	Single Input Multiple Output
SRS	Sounding Reference Signal
SSP	Small Scale Parameters
SU-MIMO	Single-user Multiple Input Multiple Output
Tanh	Hyperbolic Tangent
TDD	Time-division Duplexing

UE	User Equipment
UL	Uplink
ULA	Uniform Linear Array
ULSRS	Uplink Sounding Reference Signal
WINNER II	Wireless World Initiative New Radio II
XPR	Cross Polarization coupling power Ratio

Chapter 1

Introduction

1.1 Motivation and background

The advent of Fifth Generation (5G) technology has revolutionized the wireless communication landscape, promising ultra-high data rates, low latency, and massive connectivity. This transformative technology has, not only unlocked new possibilities for seamless communication, but has also paved the way for innovative applications that rely on the convergence of sensing and communication capabilities.

The User Equipment (UE), encompassing a wide array of smart devices such as smartphones, wearables, and Internet of Things (IoT) devices, has become an integral part of our daily lives in the 5G era. These UEs are equipped with advanced sensors, including accelerometers, gyroscopes, cameras, and environmental sensors, capable of capturing rich contextual information about the physical world.

The integration of sensing capabilities into UEs within the framework of 5G technology offers unprecedented opportunities for the development of integrated sensing and communication systems. By harnessing the power of 5G networks and leveraging the diverse sensor suite in UEs, it becomes possible to gather real-time environmental data, enable context-aware services, and support intelligent decision-making for both sensing and communication tasks.

However, the exploration of UE sensing capabilities for integrated sensing and communication in the 5G context presents unique challenges. These challenges encompass designing efficient sensing techniques that can seamlessly operate within the 5G ecosystem, optimizing resource allocation to strike a balance between sensing accuracy and communication performance, and ensuring compatibility with the stringent latency and reliability requirements of 5G applications.

Furthermore, the successful integration of sensing and communication functionalities in UEs necessitates a comprehensive understanding of the UE's sensing capabilities within the 5G paradigm. It requires addressing the interplay between sensing and communication resources, investigating the impact on network per-

formance, and considering the implications for user experience and quality of service.

Against this backdrop, our research aims to explore the UE's sensing capabilities within the context of 5G technology and investigate their feasibility for integrated sensing and communication applications. By delving into this research area, we aspire to contribute to the advancement of intelligent wireless communication systems that harness the potential of 5G networks and UE sensors, enabling enhanced user experiences, novel applications, and improved overall system performance.

1.2 Thesis Objectives and Aims

The purpose of this thesis is to address the challenges encountered in cellular communication scenarios, with a specific focus on channel estimation and Line Of Sight (LOS) detection within the context of the Orthogonal Frequency Division Multiplexing (OFDM) in cellular networks. The aims of this research project can be summarized as follows:

- Channel Transfer Function Calculation: The primary objective was to calculate the channel transfer function using the channel impulse response data from the Simulator. This calculation aims to extract valuable information about the sub-channels in the OFDM-based system. However, a significant hurdle in this step is the creation of a dataset comprising an adequate number of simulations and associated labels, which will be used to train a deep-learning model for subsequent tasks.

- Deep-Learning for LOS Detection: The second objective focuses on creating a dataset that can be used to train a deep-learning model to determine whether a channel has a line of sight or not. This information becomes particularly useful when there are obstructions between the UE and Base Station (BS). The primary aim is to train the model efficiently and generate reliable output to identify LOS and Non Line Of Sight (NLOS) scenarios accurately.

- Deep-Learning for LOS Detection with Estimated Channels: The third objective considers estimating the channel using Uplink Sounding Reference Signal (ULSRS) data. This estimation provides a comprehensive overview of the uplink channel and will eventually prove useful for scheduling on the BS. Furthermore, this information can be leveraged to assess the likelihood of transitioning from a LOS to NLOS scenario as the user moves. The goal is to estimate the channel using ULSRS data, generate a suitable dataset through simulations, and train a deep learning model. The use cases include determining UE movement direction, wall type material, arrival time to the LOS region, and the size of the blocking obstacle between the BS and UE.

By accomplishing these objectives, the thesis aims to contribute to the understanding and improvement of channel estimation techniques and LOS detection in cellular communication scenarios.
All the experiments were performed leveraging the Simulator, an emulation tool provided by *Ericsson* for analyzing the performance characteristics of the channel behavior in a wireless communication system. The research outcomes will have practical implications for optimizing system performance, enhancing network efficiency, and supporting the reliable transmission of data in complex wireless environments.

1.3 Thesis Outline

The thesis begins by providing a comprehensive introduction to the foundational theoretical background, which serves to establish a solid understanding of the subsequent research inquiry. This includes the chosen model, the Wireless World Initiative New Radio II (WINNER II) channel model, is extensively elucidated, encompassing an exploration of the specific scenarios under investigation. This entails the inclusion of path-loss formulas, and parameter definitions, and highlights the significance of incorporating deep learning techniques in the UE's link state detection process using the ULSRS, thereby contributing to the achievement of the research objectives.

Furthermore, a brief introduction of Multiple Input Multiple Output (MIMO) systems and a detailed overview of the evolutionary journey of 5G New Radio (NR) and its primary applications. The thesis then proceeds to offer an in-depth description of pivotal components within the 5G NR physical layer, with a specific focus on relevant elements such as the ULSRS, OFDM, and Time-division Duplexing (TDD).

Additionally, the thesis briefly discusses important aspects related to UE arrival time to the LOS region, the determination of UE movement direction, the identification of wall materials, and the assessment of obstacle size obstructing the communication between the UE and the BS. These aspects contribute to a more comprehensive understanding of the research scope and its implications.

The subsequent section of the thesis presents the empirical findings derived from the conducted research. The final chapter serves as a conclusive summary, encapsulating the key findings and offering a discussion on potential future paths for further investigation.

Chapter 2

General Framework

This chapter serves as a comprehensive foundation for the subsequent sections of the thesis, providing the necessary theoretical background, practical insights, and a clear link to the research objectives.

2.1 MU-MIMO

The Multi-user Multiple Input Multiple Output (MU-MIMO) channel is a transformative concept in wireless communication systems, revolutionizing data transmission and reception. By employing multiple antennas at both the transmitter and receiver and the usage of the degrees of freedom provided by the multiple antenna elements, MU-MIMO systems offer advantages such as increased data rates, improved link reliability, and enhanced spectral efficiency.

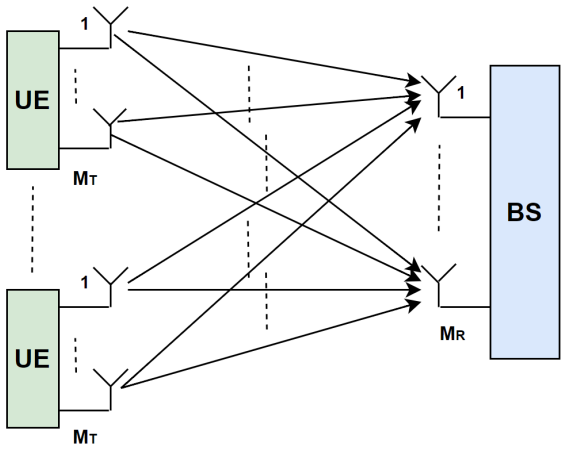

Figure 2.1: Antenna configuration in MU-MIMO systems

In contrast to Single-user Multiple Input Multiple Output (SU-MIMO) where we can only communicate with a single user at a time, using MU-MIMO we can communicate with multiple users simultaneously which increases the network capacity. Figure 2.1 depicts the uplink antenna configuration of a MU-MIMO system where M_{T} is the number of transmitter antennas per UE and M_{R} is the number of receiver antennas at the BS.

The narrowband response of a MIMO channel for a single user at subcarrier k is expressed as [1]:

$$\mathbf{y}[k] = \sqrt{\frac{E_{\mathrm{s}}}{M_{\mathrm{T}}}}\mathrm{H}[k]\ \mathbf{s}[k] + \mathbf{n}[k], \tag{2.1}$$

where $\mathbf{H}[k]$ is the MIMO channel matrix of dimension $M_{\mathrm{R}} \times M_{\mathrm{T}}$, $\mathbf{y}[k]$ is the received signal vector with dimension $M_{\mathrm{R}} \times 1$, $\mathbf{s}[k]$ is the transmit signal vector with dimension $M_{\mathrm{T}} \times 1$, $\mathbf{n}[k]$ is the $M_{\mathrm{R}} \times 1$ is the noise vector and E_s is the average transmit symbol energy. It is important to note that the average transmit symbol energy, E_s, is reduced by the number of transmitter antennas, M_{T}, to ensure a fair comparison when comparing systems with different numbers of antennas.

In the context of a multi-user environment, where the channel may be estimated using orthogonal pilots for different users, the principles of channel estimation employed in a single-user scenario can also be extended. Equation (2.2), as highlighted in our thesis, captures the relationship between a UE equipped with a single antenna ($M_{\mathrm{T}} = 1$) and a BS equipped with multiple antennas (M_{R}). This equation serves as a fundamental representation of an uplink transmission in the context of multi-user communication.

$$\mathbf{y}[k] = \sqrt{E_{\mathrm{s}}}\mathbf{h}[k]\ s[k] + \mathbf{n}[k], \tag{2.2}$$

where the channel $\mathbf{h}[k]$ is modeled by a $M_{\mathrm{R}} \times 1$ vector, $\mathbf{y}[k]$ is the received signal vector with dimension $M_{\mathrm{R}} \times 1$, , $s[k]$ is the transmit signal with $M_{\mathrm{T}} = 1$, E_s is the average transmit symbol energy and $\mathbf{n}[k]$ is the $M_{\mathrm{R}} \times 1$ is the noise vector. It is important to note that in Single Input Multiple Output (SIMO) systems, the number of transmit antennas (M_{T}) is 1, and therefore, only E_s is considered as the average transmit symbol energy.

For effective channel estimation, we employed ULSRS ($p[k]$) transmitted from the UE to the BS. By substituting the variable s with p in Equation (2.2), the resulting equation can be expressed as follows:

$$\mathbf{y}[k] = \sqrt{E_{\mathrm{s}}}\mathbf{h}[k]\ p[k] + \mathbf{n}[k]. \tag{2.3}$$

In Equation (2.3), the channel estimation is performed using the ULSRS pilot represented by the variable $p[k]$. The channel vector $\mathbf{h}[k]$, the transmit signal $p[k]$, and the noise vector $\mathbf{n}[k]$ collectively contribute to the overall equation, reflecting the relationship between the received signal ($\mathbf{y}[k]$) and the channel characteristics.

After the transmitted signal (ULSRS) is received by the BS and its characteristics are known, the channel estimation ($\mathbf{h}[k]$) process can commence. This process leverages the specific characteristics of the 5G NR system. Details of this procedure will be outlined in the subsequent chapters. This thesis primarily centers on detecting the link state of the UE in a system, the goal is to accurately distinguish between two conditions: NLOS and LOS. To achieve this, it is essential to have a function that can effectively analyze the characteristics of the channel.

$$f(\hat{\mathbf{h}}[k]) = \begin{cases} \text{LOS} \\ \text{NLOS} \end{cases}, \tag{2.4}$$

where $\hat{\mathbf{h}}[k]$ is the estimated channel.

The methodology for identifying channel characteristics can be approached in various manners. In this investigation, machine-learning techniques are employed to detect the link state of one UE. Understanding the link state of UE offers several practical applications, such as resource scheduling and beamforming strategies. The results can be exploited for multi-UE scenarios as well, the only difference is that there may be worse estimates of the channel due to interference from other users and noise. Some of these applications will be thoroughly examined within the framework of this thesis.

Chapter 3

WINNER II Channel Model

The simulations in this thesis are based on the WINNER II channel model. The following sections provide a full overview of this channel model.

The WINNER II channel model represents a notable progression in the field of signal propagation analysis, particularly in diverse scenarios. It builds upon the foundation of WINNER I, offering expanded scenarios, wider frequency coverage, and enhanced customization of antenna characteristics. The model employs rigorous principles of geometry and probability to understand signal behavior over time, accounting for propagation factors and antenna interactions. By incorporating real measurement statistics, it enables precise analysis and valuable insights for wireless communication research and design. Overall, the WINNER II model serves as a valuable tool for unraveling the complexities of signal propagation and optimizing wireless communication systems.

3.1 Some radio channel properties

In this section, some definitions that are very useful for understanding the channel dynamics in the context of our research project are discussed. Initially, certain properties of radio channels are explained. Large-scale fading occurs due to interactions with objects that are significantly larger than the wavelength of the signal. These objects obstruct the signal's path to the receiver. On the other hand, small-scale fading results from objects reflecting, diffracting, or refracting the signal. This leads to multipath propagation between the transmitter and the receiver, causing constructive and destructive interference.

3.1.1 Large Scale Parameters

- **Delay Spread (DS)**: The difference in arrival times between a signal's earliest and latest major components. It describes the dispersion of signal energy over time caused by multipath propagation and influences the extent of ISI in the communication system.

- **Angle Spread (AS)**: Angle spread refers to the variation in the direction or angle of arrival of signals at a receiver in a wireless communication system. It characterizes the spread of signal energy across different angular paths due to scattering, reflections, and diffractions in the propagation environment.
- **Shadow Fading (SF)**: Shadow fading occurs when the channel's coherence time significantly exceeds the delay constraints of the application, resulting in relatively stable amplitude and phase variations over the operational duration. This phenomenon typically arises when substantial obstacles, like hills or large buildings, obstruct the primary signal path between the transmitter and receiver. The impact of shadow fading on received power is commonly characterized by a log-normal distribution with a standard deviation aligned with the log-distance path loss model.
- **Rician factor (K)**: The ratio of the power in the LOS component to the power in the diffuse component is called as Rician factor (K). If $K \rightarrow 0$, the Rice distribution becomes the Rayleigh distribution.

3.1.2 Small Scale Parameters

- **Path delays**: Path delay, also known as propagation delay, refers to the time it takes for a signal to travel from a transmitter to a receiver along a specific communication path. In wireless communication systems, signals propagate through the air, guided by various propagation mechanisms such as LOS propagation, reflection, diffraction, and scattering.
- **Angle of Arrival (AoA)**: The angle of arrival refers to the angle at which a signal approaches a receiving antenna in relation to a specified reference axis, such as the normal to the surface of the antenna.
- **Angle of Departure (AoD)**: The angle of departure describes the direction from which a radio wave is transmitted by a transmitting antenna. It represents the angle at which a transmitted signal departs the transmitting antenna in relation to a reference axis.
- **Cross Polarization coupling power Ratio (XPR)**: It is a metric used to assess the degree of polarization discrimination in an antenna system. It describes how an antenna designed to transmit or receive a specific polarization (e.g., vertical or horizontal) is influenced or sensitive to orthogonal polarization signals.

In the next section, the WINNER II channel model and its related parameters are discussed in detail.

3.2 WINNER II channel model

The WINNER II channel model includes 12 indoor and outdoor propagation scenarios, as well as the ability to simulate LOS and NLOS propagation circum-

stances. It is also implemented in MATLAB™ and it is capable of deploying MIMO setups.

WINNER II channel model generates the time-variant channels, however, only one snapshot of the channel is considered in this study, assuming that the run-times do not change with time (this occurs when neither transmitter nor interacting objects move) [2]. The Channel Impulse Response (CIR) is:

$$\mathbf{h}(\tau) = \sum_{n=0}^{N-1} \boldsymbol{\alpha}_n \cdot \delta(\tau - \tau_n), \tag{3.1}$$

where N is the number of delay clusters, and τ_n is the delay of the cluster n, and $\boldsymbol{\alpha}_n$ is a vector of complex values.

A Fourier transformation of the impulse response in Equation (3.1) gives the transfer function $\mathbf{H}(f)$:

$$\mathbf{H}(f) = \mathcal{F}\{\mathbf{h}(\tau)\}, \tag{3.2}$$

3.2.1 Path delay (τ) calculation

Delays are drawn randomly from the delay distribution defined in [3]. The model incorporates two distinct delay distributions that vary depending on the scenario: exponential delay distribution and uniform delay distribution. When using the exponential delay distribution:

$$\tau'_{\mathrm{n}} = -\mathrm{r}_\tau \sigma_\tau \ln(\mathrm{X_n}), \tag{3.3}$$

where r_τ is the delay distribution proportionality factor, σ_τ is delay spread, $\mathrm{X}_n \sim$ Uni(0,1) and cluster index n = 1,....,N. With uniform delay distribution the delay values τ'_n are drawn uniformly from the corresponding range $\tau \sim \mathrm{Uni}(\tau_{\min}, \tau_{\max})$.

It's crucial to emphasize that the WINNER II channel model generates the channel impulse response, which consists of multiple normalized delay clusters. To normalize the delays, we subtract the minimum delay from each of the delays and then arrange them in descending order, which is expressed as:

$$\tau_{\mathrm{n}} = \mathrm{sort}(\tau'_{\mathrm{n}} - \min(\tau')_{\mathrm{n}}). \tag{3.4}$$

This way, the delay of the first arriving cluster is always set to zero.

In LOS, additional scaling of delays is required to compensate for the effect of the LOS peak added to the delay spread. The scaling constant D is Ricean K-factor dependent and it is determined by Equation (3.5).

$$\mathrm{D} = 0.7705 - 0.0433\mathrm{K} + 00002\mathrm{K}^2 + 0.000017\mathrm{K}^3, \tag{3.5}$$

where K [dB] is the Ricean K-factor defined in [3]. The scaled delays are then given by

$$\tau_{\mathrm{n}}^{\mathrm{LOS}} = \frac{\tau_{\mathrm{n}}}{\mathrm{D}}, \tag{3.6}$$

3.2.2 Cluster power (P) calculation

The cluster powers are calculated assuming a single slope exponential Power Delay Profile (PDP). Power assignment depends on the delay distribution defined in [3]. With exponential delay distribution, the cluster powers are determined by

$$\mathrm{P'}_n = \exp\left(-\tau_n \frac{\mathrm{r}_\tau - 1}{\mathrm{r}_\tau \sigma_\tau}\right) \cdot 10^{\frac{-Z_n}{10}} \tag{3.7}$$

and with uniform delay distribution they are determined by

$$\mathrm{P'}_n = \exp\left(\frac{-\tau_n}{\sigma_\tau}\right) \cdot 10^{\frac{-Z_n}{10}}, \tag{3.8}$$

where $Z_n \sim \mathrm{N}(0, \sigma^2)$ is the per cluster shadowing term in [dB]. The power is then normalized so that the total power of all clusters is equal to one, i.e.,

$$\mathrm{P}_n = \frac{\mathrm{P'}_n}{\sum_{n=1}^{N} \mathrm{P'}_n} \tag{3.9}$$

The power of each ray within a cluster is given by P_n / M, where M is the number of Multipath Components (MPC) per cluster.

3.2.3 AoA(ψ) & AoD (ϕ) calculation

If the composite Power Azimuth Spectrum (PAS) of all clusters is modelled as wrapped Gaussian (see Table 4-5 [3]) the AoA are determined by applying inverse Gaussian function with input parameters P_n and RMS angle spread σ_ψ

$$\psi'_n = \frac{2\sigma_{\mathrm{AoA}} \sqrt{-\ln\left(\mathrm{P}_n / \max(\mathrm{P}_n)\right)}}{\mathrm{C}}, \tag{3.10}$$

where $\sigma_{\mathrm{AoA}} = \sigma_\psi$ /1.4 is the Standard Deviation (SD) of arrival angles (the value 1.4 is the ratio of Gaussian SD and corresponding "RMS spread"). Constant C is a scaling factor related to the total number of clusters and is given in the Table 3.1:

#Clusters	C
4	0.779
5	0.860
8	1.018
10	1.090
11	1.123
12	1.146
14	1.190
15	1.211
16	1.226
20	1.289

Table 3.1: Number of clusters and corresponding constant (C) Values for AoA calculation

For AoDs (ϕ_n) the procedure is analogous.

3.2.4 XPR calculation

The calculation of cross polarisation power ratios (XPR) K for each ray m of each cluster n is given in Equation (3.11).

$$K_{m,n} = 10^{\mathrm{X}/10}, \tag{3.11}$$

where $m = 1, \ldots, M$ is the ray index, $\mathrm{X} \sim \mathrm{N}(\mu,\sigma^2)$ is Gaussian distributed with μ and σ given in [3] for XPR.

3.2.5 Path-loss

Path-loss (PL) is the reduction in signal strength that occurs as a radio wave travel through a medium, such as air or buildings, from a transmitter to a receiver. It is a fundamental concept in wireless communication systems and is influenced by various factors, including distance, frequency, obstacles, and environmental conditions. The basic PL formula which is used in WINNER II channel model is [3],

$$PL = A\ log_{10}(d[m]) + B + C\ log_{10}\left(\frac{f_c[GHz]}{5.0}\right) + X, \tag{3.12}$$

where A is the parameter corresponding to the path-loss exponent, d is the distance between the transmitter and the receiver in [m], B is also a parameter that depends on the frequency and antenna height, C scales the path-loss frequency dependence, f_c is the system frequency in the frequency range of 2 to 6 GHz, and X is an environmental specific term which is scenario dependent. The distribution of the shadow fading is log-normal, and the SD is different for each propagation condition with respect to each scenario.

3.3 Channel coefficient generation using WINNER II channel model

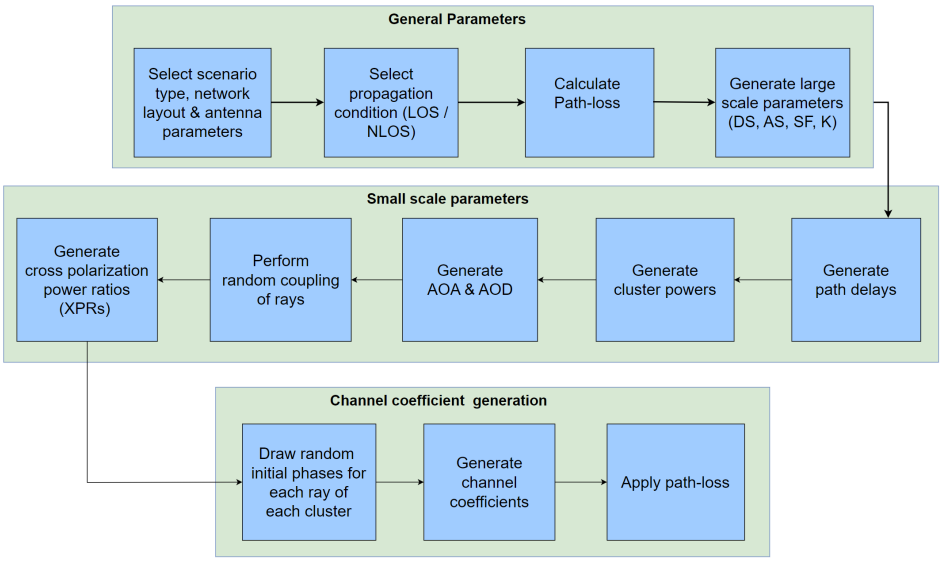

Figure 3.1: Channel coefficient generation using WINNER II channel model

The generation of channel coefficients in this study is carried out through a three-stage process. The initial stage involves the initialization of general parameters specific to the WINNER II channel model. This encompasses the selection of a scenario type, such as C1 or A1 (which will be explained later in detail), as well as the configuration of the network layout, including the number and positions of UEs and BSs within the Geographic Coordinate System (GCS). Moreover, antenna parameters, such as the type of antenna array structure employed in the simulation (in this case, a Uniform Linear Array (ULA) with $\lambda/2$ antenna spacing), and array geometry are defined. To accurately model the channel, propagation conditions are assigned, distinguishing between LOS and NLOS scenarios. The PL is subsequently computed using the equations within each scenario. The LSPs have been generated based on the equations specified in reference [3]. It is important to note that the number of clusters may vary between 8 and 24 according to the scenario. However, the number of MPCs remains constant at 20 in the WINNER II channel model.

During the second stage, the SSPs are generated. Notably, in the process of generating SSPs, the LSPs are utilized as control parameters, effectively influencing the characteristics of the small-scale fading. As the final stage of the channel coefficient generation process, the WINNER II channel's impulse response is constructed by incorporating the specifications defined by the 3GPP. This is achieved by leveraging the LSPs and SSPs in accordance with the prevailing WINNER II

framework. The channel impulse response is generated using the following formula:

$$\mathbf{h}(t,\tau) = \sum_{n=1}^{N} \mathbf{h}_n(t,\tau), \tag{3.13}$$

Where N represents the number of distinct paths for each scenario, t and τ are variables indexing the time and delay domains. Note that, as previously mentioned, the CIR varies depending on specific scenarios and propagation conditions (as outlined in Table 3.2). Assuming time invariance throughout a transmission interval, we can drop the channel dependency on t within each interval and use Equation (3.1) to obtain a channel realization. For readers seeking a more in-depth understanding of the intricacies involved in channel realization, we recommend referring to the work cited as [3].

The following Table 3.2 provides a concise summary of the number of clusters for LOS and NLOS under the different scenarios considered in this thesis.

Scenario	**# Clusters**	
	LOS	NLOS
C1	15	14
A1	12	16

Table 3.2: Number of clusters for different scenarios

In order to visually illustrate the key components of a MIMO channel, Figure 3.2 sourced from [3] is presented. This figure depicts the essential elements involved in a MIMO channel, including the antenna arrays located at both ends of the connection and the propagation paths.

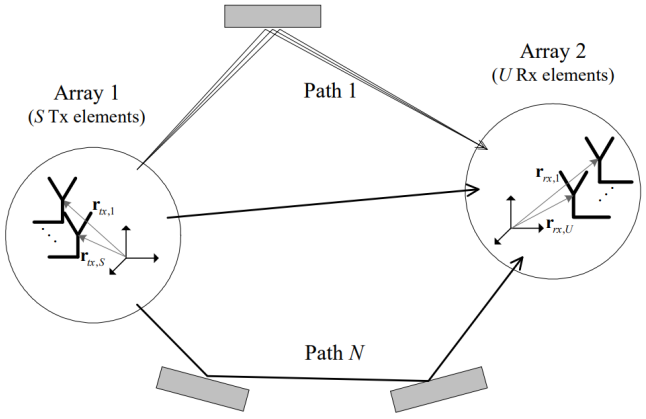

Figure 3.2: The MIMO channel

In this thesis, we studied two scenarios: A1 and C1. The following provides detailed information on each scenario [3].

3.3.1 A1 scenario

The investigated scenario was an **indoor-to-indoor** configuration, involving a communication system with a BS and a UE situated in the indoor corridors. The experimental setup distinguished between LOS and NLOS propagation conditions based on the location of the UE within the indoor environment. This placement ensures coverage within the indoor spaces, particularly along the corridors where users are expected to be present (see Figure 3.3). If the UE is in the same corridor as the BS, it experiences LOS propagation conditions. LOS occurs when there is a direct, unobstructed path between the BS and the UE. If the UE is positioned in a perpendicular corridor adjacent to the corridor where BS is situated, it encounters NLOS propagation conditions. NLOS occurs when the direct line of sight between the transmitter and receiver is obstructed by the obstacles such as walls or partitions.

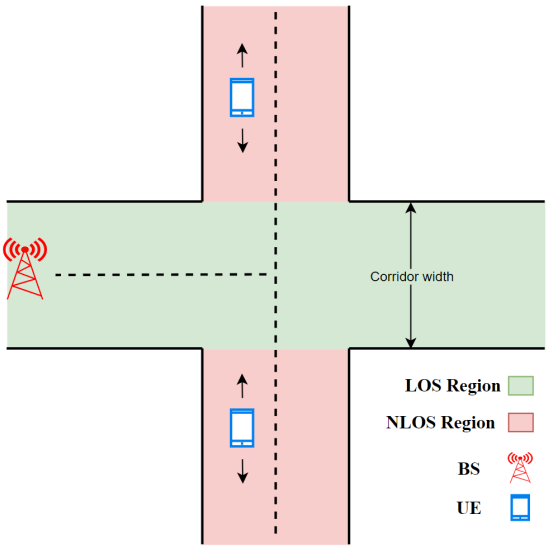

Figure 3.3: Layout for A1 scenario

In LOS conditions, signals travel directly from the BS to the UE without significant obstruction. The PL in LOS scenarios may be lower compared to NLOS due to the absence of obstacles in the main communication path. In NLOS conditions, signals experience additional attenuation and reflection due to interactions with obstacles such as walls or partitions. This results in an increased PL and potentially degraded signal quality. This model considers factors such as distance between the transmitter and receiver, free space path loss, and antenna characteristics. In NLOS scenarios, additional losses due to walls or obstructions are

considered. This scenario assumes that the floors within the indoor environment are identical in structure and layout. This assumption simplifies the propagation modeling and allows for consistent analysis across different areas of the building. Figure 3.3 provides a full overview of the above scenario.

3.3.1.1 PL for LOS & NLOS in A1 scenario

According to the Equation (3.12), the PL calculations for LOS and NLOS propagation conditions can be expressed as follows:

$$PL_{\text{LOS}} = 18.7\ log_{10}(d[m]) + 46.8 + 20\ log_{10}\left(\frac{f_c}{5.0}\right), \tag{3.14}$$

where SD of the Shadow Fading (SF) 3 dB and distance d in the range of 3 to 100 m. 18.7, 46.8, and 20 are the A, B, and C parameter values for LOS propagation. The height of the BS (h_{BS}) and Mobile Station (MS) (h_{MS}) must be in the range of 1 to 2.5 m.

$$PL_{\text{NLOS}} = 36.8\ log_{10}(d[m]) + 43.8 + 20\ log_{10}\left(\frac{f_c}{5.0}\right) + X, \tag{3.15}$$

where 36.8, 43.8, and 20 are the A, B , and C parameter values for NLOS propagation and X is influenced by the number of walls (n_w) between the BS and the UE as well as the type of wall material. For light walls, we have X = 5(n_w -1), considering a 5 dB loss associated with each light wall. On the other hand, for heavy walls, we have X = 12(n_w - 1), accounting for a 12 dB loss per heavy wall. The light wall material is e.g., plasterboard, and the heavy wall material is e.g., brick or concrete. It is important to note that the value of n_w must be greater than zero to indicate a NLOS propagation condition and we have considered $n_w = 2$ in this study.

3.3.2 C1 scenario

This scenario considers a **suburban macro-cell** environment, with the BS positioned above a rooftop and the UE is located at street level, as depicted in Figure 3.4. When the UE is located at street level without any obstructing structures, such as buildings or vegetation, LOS propagation can be observed; otherwise, NLOS propagation occurs. Macro-cells typically cover larger areas compared to micro-cells and suburban environments are characterized by a mix of residential, commercial, and open spaces. The buildings within this zone are described as low-rise residential structures, primarily consisting of detached houses with one or two floors. The vegetation in the area is described as growing in a restrained or moderate way. This suggests that the plant cover is not excessively dense or lush, but rather moderate in its growth.

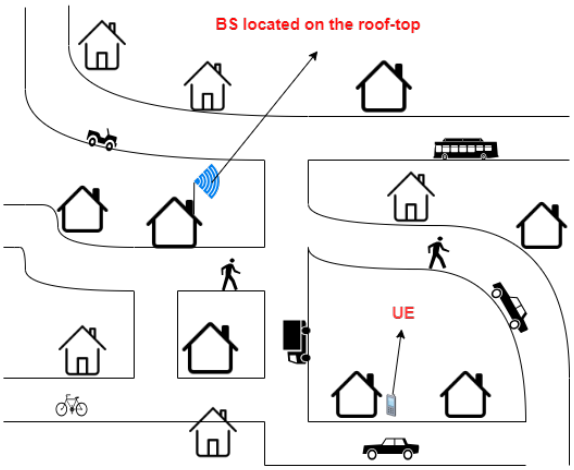

Figure 3.4: Layout for C1 scenario

3.3.2.1 PL for LOS & NLOS in C1 scenario

The PL calculations from Equation (3.12) for LOS and NLOS propagation conditions, can be computed as follows:

$$PL_{\text{LOS}} = 23.8\ log_{10}(d[m]) + 41.2 + 20\ log_{10}\left(\frac{f_c}{5.0}\right) \tag{3.16}$$

or

$$\begin{aligned} PL_{\text{LOS}} &= 40.0\ log_{10}(d[m]) + 11.65 - 16.2\ log_{10}(h_{\text{BS}}[m]) \\ &\quad - 16.2\ log_{10}(h_{\text{MS}}) + 3.8\ log_{10}\left(\frac{f_c}{5.0}\right), \end{aligned} \tag{3.17}$$

where f_c is the carrier frequency in GHz. Equation (3.16) is utilized for calculations when 30 m $< d <$ d_{BP} and Equation (3.17) is applied for distances ranging when $d_{\text{BP}} < d <$ 5 km where d_{BP} is the break point distance and is computed as follows: $d_{\text{BP}} = 4\ h_{\text{BS}}\ h_{\text{MS}}\ f_c/\text{c}$. The A, B, and C parameter values are different for LOS propagation in Equations (3.16) and (3.17) and are dependent on d. The height of the BS (h_{BS}) and MS (h_{MS}) is considered as 25 m and 1.5 m and c is the speed of light.

$$\begin{aligned} PL_{\text{NLOS}} &= (44.9 - 6.55\ log_{10}(h_{\text{BS}}[m])\ log_{10}(d[m]) + 31.46 + 5.83\ log_{10}(h_{\text{BS}}[m]) \\ &\quad + 23\ log_{10}\left(\frac{f_c}{5.0}\right), \end{aligned} \tag{3.18}$$

where distance d is 50 m < d < 5km and the remaining parameters are defined as in LOS propagation condition.

Chapter 4

5G NR Overview

This section highlights the physical layer characteristics of NR that are crucial for understanding the thesis work. It is worth noting that a comprehensive understanding of the uplink and downlink operations holds immense significance in ensuring the maximum efficacy of the MATLAB™ simulation model implemented in the project.

4.1 Introduction

NR, developed by 3rd Generation Partnership Project (3GPP) as the global standard for 5G networks, is a Radio Access Technology (RAT) based on OFDM. OFDM is chosen for its robustness to time dispersion and ability to exploit both time and frequency domains for defining channel and signal structures. NR operates in two frequency ranges: Frequency range 1 (FR1) from 0.45 GHz to 6 GHz, and Frequency range 2 (FR2) from 24.25 GHz to 52.6 GHz. Unlike LTE, where all devices support a maximum carrier bandwidth of 20 MHz, NR allows for wider bandwidths. The transmission numerologies in NR vary based on the Subcarrier Spacing (SCS) i.e, Δf, and Cyclic Prefix (CP) lengths. According to the information provided in Table 4.1, the normal CP configuration comprises a fixed number of 14 symbols per slot, whereas the extended CP configuration consists of 12 symbols per slot.

μ	$\Delta f = 2^{\mu} \cdot 15$[kHz]	**Cyclic prefix**
0	15	Normal
1	30	Normal
2	60	Normal, Extended
3	120	Normal
4	240	Normal

Table 4.1: 5G numerologies with different carrier spacings & CP

4.2 OFDM

Orthogonal Frequency Division Multiplexing (OFDM) is a modulation scheme widely used in modern telecommunication systems for transmitting digital data over wireless, optical, and wired communication channels. It converts a high-rate data stream into a number of low-rate data streams that are transmitted over parallel, narrowband channels that can be easily equalized. It plays a crucial role in 5G NR because of its high spectral efficiency, resilience to fading, resource allocation flexibility, support for Massive MIMO, and low-complexity equalization. Consequently, it serves as the fundamental transmission scheme for both the downlink and uplink transmission paths in NR.

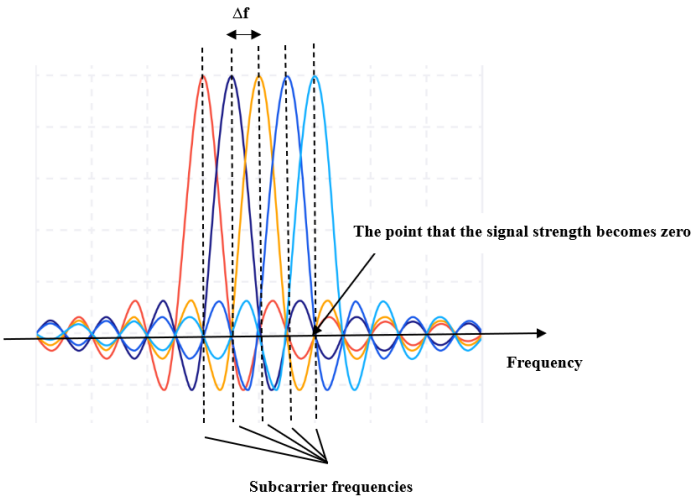

Figure 4.1: OFDM with subcarrier spacing Δf

Figure 4.1 shows the frequency spectrum of an OFDM signal. To ensure the separation of signals carried by different subcarriers, orthogonality is achieved by spacing the subcarriers carefully, with a subcarrier spacing $\Delta f = W/(N+1)$, where W represents the total available bandwidth, and N corresponds to the number of subcarriers and the center frequency. Using this approach we can analyze how different values of W, and N affect the allocation and utilization of bandwidth resources in the wireless communication system.

4.2.1 Cyclic Prefix

The incorporation of a Cyclic Prefix(CP) in the OFDM modulation scheme enhances its resilience. The CP, consisting of samples appended to each OFDM symbol, serves to mitigate Inter Symbol Interference (ISI) and ensure the accuracy of the Fast Fourier Transform (FFT). By converting the convolution in the

temporal domain to a circular convolution, the CP enables simplified channel estimation and equalization in the frequency domain, showcasing a distinct advantage of OFDM technology.

4.3 TDD

TDD is a communication technique where the transmission and reception of signals occur in different time slots within the same frequency band [4]. Many 5G NR deployments exclusively utilize TDD due to its advantages in spectrum allocation flexibility, reduced latency, channel reciprocity, and management of asymmetric traffic loads. TDD systems often utilize uplink training and reciprocity to obtain Channel State Information (CSI) and can be implemented in various configurations, such as multi-cell systems or very large MIMO arrays.

4.4 NR time-domain structure

In the time domain, NR transmissions are structured into 10 ms frames, each of which is divided into 10 equally sized subframes of 1 ms duration. A subframe is then divided into slots consisting of 14 OFDM symbols each i.e., the duration of a slot in milliseconds depends on the numerology (μ). The slot structure for higher SCSs in NR is then derived by scaling this baseline structure by powers of two (2^{μ}).

In our research, we have employed a SCS (Δf) of 15 kHz, based on numerology $\mu = 0$. Although numerology 1 ($\mu = 1$) was an alternative, $\mu = 0$ was preferred to enable coexistence and compatibility with Long Term Evolution (LTE) systems. For $\mu = 0$, the slot duration equals to the subframe duration, as shown in Figure 4.2, facilitating smooth integration with the existing LTE infrastructure.

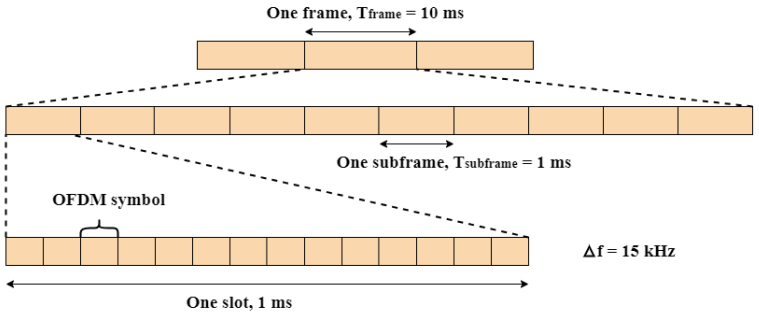

Figure 4.2: 5G NR frame structure for numerology, $\mu = 0$

4.5 ULSRS and its significance in 5G

The use of Sounding Reference Signal (SRS) depends on the specific requirements of the network deployment and the features supported by the devices and infrastructure. The reason for SRS importance in NR is due to the fact that TDD technology is the primary mode of deployment. In TDD, both Uplink (UL) and Downlink (DL) transmissions occur in the same frequency band, but at different times. This means that the BS can leverage the channel estimation outcome from SRS not only for UL processing but also for DL pre-processing, based on channel reciprocity. This is crucial in TDD mode because the BS needs to estimate the CSI for both UL and DL transmissions to optimize the use of the available resources. These SRS signals serve a variety of critical purposes and are an essential component of the network's smooth operations [5].

- The transmission of uplink SRS by the UE enables the BS to estimate vital channel characteristics such as frequency response and time delay spread. This estimation is crucial for optimizing communication quality by adjusting transmission parameters, such as the power of each antenna element. [6].
- Furthermore, the information derived from uplink SRS assists the BS in dynamically scheduling transmissions and allocating resources. By prioritizing users with favorable channel conditions and avoiding fast fading in the frequency domain, network performance is enhanced for all users [7].
- Moreover, uplink SRS signals help the BS distinguish between desired UE signals and interference, thereby improving system performance and spectral efficiency [8]. Adaptive strategies, guided by SRS signals, effectively mitigate interference, enhancing communication reliability and throughput.
- Additionally, uplink SRS signals aid the BS in CSI estimation for beamforming in MIMO systems. This enhances signal reception and data rates by directing energy towards intended UEs, reducing interference, and ultimately improving communication reliability and throughput [9].

4.5.1 Uplink SRS (ULSRS) frame structure

A device can be configured to send out SRS to perform uplink channel sounding. SRS can be interpreted as the uplink counterpart to downlink CSI Reference Signals (CSI-RS) , as they both use channel sounding but in opposing transmission directions. SRS is restricted to four antenna ports and typically covers one, two, or four consecutive OFDM symbols, and our thesis focuses on 4 OFDM symbols for SRS. The structural configuration of SRS is characterized by a comb-like arrangement, wherein the signal is transmitted exclusively on selected subcarriers within the frequency domain, at intervals of either two or four, delineating the comb-2 and comb-4 patterns, respectively. The Physical Resource Blocks (PRBs) represent the fundamental units of radio resources utilized for actual data transmission and reception in the wireless system. These PRBs, which are the Resource

Blocks(RBs), serve as the basic allocation and scheduling elements for efficient spectrum utilization. Figure 4.3 depicts the frame structure of ULSRS with one Resource Block (RB). The structure displays subcarriers in the frequency domain and 14 OFDM symbols (one slot or subframe) in the time domain, utilizing the comb-2 SRS structure. The SRS is typically restricted to four antenna ports, which can be utilized by four separate UEs through cyclic shifts, a process of changing the phase in the frequency domain. The SRS periodicity, set by the network designer, determines the time intervals at which UEs transmit their ULSRS signals. For the purposes of our research, we have considered an SRS periodicity of 5 milliseconds.

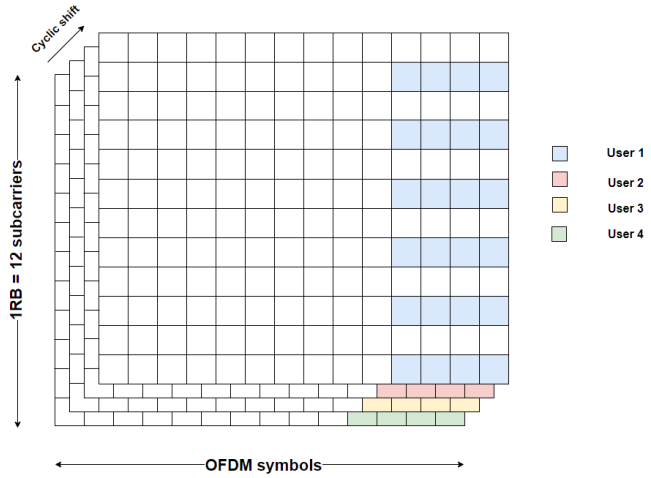

Figure 4.3: ULSRS frame structure with comb-2 configuration

4.5.2 Channel estimation using Uplink SRS

As mentioned in Section 4.5 about the significance of ULSRS in 5G, estimating the channel using ULSRS from a UE is extremely important when we have frequency selective wireless channel which varies over time. One way of estimating the channel is to insert known sequences of data in the transmitted signal. NR uses such pilot aided estimation in the frequency domain by mapping reference symbols, like ULSRS onto the resource grid, as illustrated in Figure 4.3.

The ULSRS is transmitted from the UE to the BS through a channel via the uplink sendframe (UL sendframe). The BS captures the uplink receiveframe (UL receiveframe) to obtain the transmitted SRS signal for further processing. By dividing the UL sendframe with UL receiveframe we can estimate the channel (Equation (4.1)). However, initially, these estimates are available only for a subset of the resource grid. Interpolation techniques are employed to extend the channel estimates to the entire resource grid. These techniques utilize the existing channel estimates as reference points and interpolate the channel response across the re-

maining grid points. By applying interpolation, a comprehensive set of channel estimates ($\hat{\mathbf{h}}$) is obtained, facilitating a more comprehensive characterization of the channel across the entire resource grid.

$$\hat{\mathbf{h}} = \frac{\text{UL receiveframe}}{\text{UL sendframe}} \tag{4.1}$$

4.6 Coherence Bandwidth and Delay Spread

Here as an example, by calculating path delays using equations in Section 3.2.1, we can estimate the coherence bandwidth (B_{coh}). B_{coh} was estimated by applying the equations detailed in Section 3.2.1 to calculate path delays. B_{coh} represents the frequency range in which the channel approximately exhibits frequency-flat fading meaning that the channel response is relatively constant across that bandwidth. It is determined by the delay spread of the channel, which refers to the spread in propagation delay between the earliest and latest multi-path components. In the context of the C1 scenario, the following Tables 4.2 and 4.3 were generated through calculations performed using the Simulator. It is crucial to note that, according to the reference provided in [3], each cluster for the given scenario is characterized by a single path delay. These tables provide relevant data for further analysis.

Cluster	1	2	3	4	5	6	7	8	9	10	11	12	13	14	15
Path Delay(ns)	0	0	0	5	5	10	10	15	15	25	25	25	45	45	45

Table 4.2: Clusters and corresponding normalized path delays for C1 scenario in LOS propagation condition

Cluster	1	2	3	4	5	6	7	8	9	10	11	12	13	14
Path Delay(ns)	0	10	20	65	85	125	140	145	180	280	330	360	535	635

Table 4.3: Clusters and corresponding normalized path delays for C1 scenario in NLOS propagation condition

From the Tables 4.2 and 4.3, B_{coh} is calculated using the following formula:

$$B_{\text{coh,LOS}} = \frac{1}{\tau_1 - \tau_{15}} = 22.2 \text{ MHz} \tag{4.2}$$

$$B_{\text{coh,NLOS}} = \frac{1}{\tau_1 - \tau_{14}} = 1.57 \text{ MHz} \tag{4.3}$$

It is observed that in LOS propagation conditions, the B_{coh} is high due to a reduced delay spread, simplifying signal processing and reducing the likelihood of ISI. However, in NLOS propagation conditions with a larger delay spread, the

B_{coh} is low, posing challenges in signal detection and decoding. Understanding this relationship is crucial for selecting suitable modulation and coding schemes, resource allocation strategies, and channel equalization techniques to optimize system performance. Notably, when employing OFDM, the use of subcarriers and guard intervals effectively mitigates the impact of ISI, making it less of a concern.

Chapter 5

Deep Learning

In this chapter, we delve into the intricate details of the deep learning methods and their significance in our thesis work. We explain how deep learning algorithms are a subset of machine learning that enables machines to learn and perform complex tasks without being explicitly programmed. We also discuss convolutional neural networks and their applications. Additionally, we highlight the importance of deep learning in our thesis work, and how it can help us to achieve our research objectives.

5.1 Deep learning

Deep learning is a part of Machine Learning (ML) and is based on Artificial Neural Network (ANN) architectures, where it uses layers of interconnected nodes called neurons that work together to process and learn from the input data. In a fully connected Deep Neural Network (DNN), there is an input layer and one or more hidden layers connected one after the other [10]. The output of one neuron becomes the input to other neurons in the next layer of the network, and this process continues until the final layer produces the output of the network. The layers of the neural network transform the input data through a series of nonlinear transformations, allowing the network to learn complex representations of the input data.

The following Figure 5.1, gives an overview of an ANN architecture. According to [11], one of the most significant benefits of deep learning is its ability to automatically learn feature representation at multiple levels of abstraction.

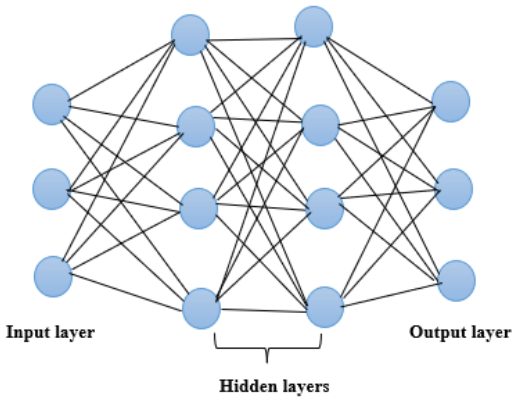

Figure 5.1: Artificial Neural Network Architecture

5.2 Flow Chart Of Deep Learning

The flow chart of deep learning, depicted in Figure 5.2, involves several important steps. It begins with acquiring the initial data set, which is then cleaned to remove any irrelevant or incorrect data points. The cleaned data is then transformed into a format suitable for training the model. Additionally, data reduction techniques may be applied to reduce the size or complexity of the data.

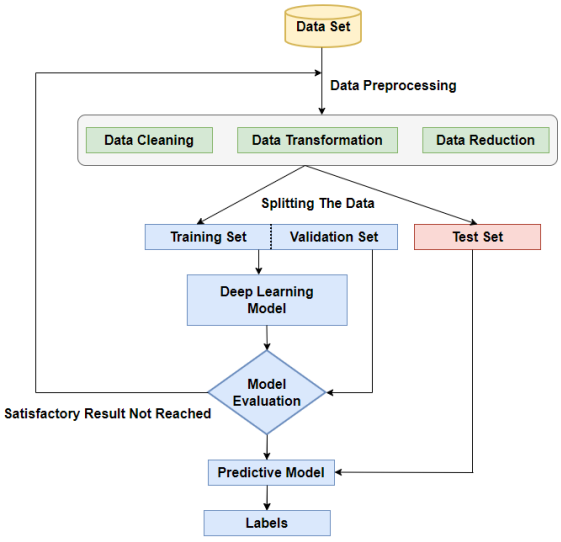

Figure 5.2: Flow Chart of Deep Learning

After the data transformation and potential reduction, the data set is divided into three subsets: the training set, the validation set, and the test set. In this thesis, a training set comprising around 70% of the data is used to train the deep learning model and adjust its parameters. A validation set, consisting of approximately 10% of the data, is employed to fine-tune the model's hyper parameters and evaluate its performance during training. The remaining 20% of the data is reserved for the test set, which serves to assess the final performance of the trained model.

5.2.1 Fundamental Concepts in Deep Learning

Two fundamental concepts in the training process are loss and epochs. Once the data is partitioned, the deep learning model is built and trained using the training set. The model's parameters are adjusted iteratively to update its parameters based on batches of training samples, referred to as epochs. The training process is typically divided into a series of epochs. Training for multiple epochs allows the neural network to gradually converge towards an optimal solution [12].

Loss refers to a quantitative measure of the deviation between the predicted output of a neural network and the actual target output during the training phase [13]. The model is evaluated to determine its performance against predefined criteria. By optimizing the loss function, the neural network adjusts its parameters to minimize prediction errors. The trained model is then used to make predictions on the unseen test set. The model takes input from the test set and generates output labels or values as the final results.

As stated in reference [14], the training of deep learning models is not compatible with complex values. However, as will be described in the next chapter, the channel estimates are complex values. Therefore, to address this limitation, a pre-processing step was implemented to separate the complex values into their constituent real and imaginary parts.

In the pursuit of identifying the optimal classification through neural networks and ensuring its validity, the primary challenge encountered is that of overfitting. This phenomenon occurs when the model's error concerning the input data approaches zero, indicating near-perfect performance. However, it is crucial to acknowledge that in neural networks, overfitting can manifest when the model exhibits low bias but high variance. Overfitting results from an excessively precise or complex model, which becomes evident when there is a minimal training error alongside a significantly high validation error. Typically, overfitting arises from one of the following factors:

- The existence of outliers in the input set causes the high variance of network parameters.
- The use of overly complex resolution algorithms in ML can lead to overfitting, where the model becomes excessively specialized to the training data, compromising its ability to generalize to new inputs.
- When the number of data used in training is too high [15].

5.2.2 Convolutional Neural Networks

Convolutional Neural Network (CNN) is an extended version of ANN that has emerged as a powerful tool used in a wide range of applications, including computer vision [16], speech recognition [17], identification of albuminous sequences in bioinformatics [18] and many others. At the same time, CNNs are very demanding in terms of the hardware and time cost of a computing system, which considerably restricts their practical use, e.g., in embedded systems, real-time systems, and mobile devices [19]. CNNs are designed to automatically identify and extract relevant features from the data through the use of convolutional layers [20]. Convolutional layers apply a set of filters to the input data, identifying patterns and features. These features are then passed on to fully connected layers.

Within the scope of this study, the simulations were conducted employing WINNER II channel models, considering a CNN architecture to estimate the function f from Equation (2.4), to detect the UE's link state. The inputs (a vector of samples of the frequency response) and outputs (human-labeled) were matched to train a model. The CNN model utilized in this study employed various layers, including the input layer, convolutional layers, pooling layers, and fully connected layers [21]. These layers will be briefly described in the following section, offering a concise explanation of their respective functions and their overall importance within the model.

5.2.2.1 CNN architecture

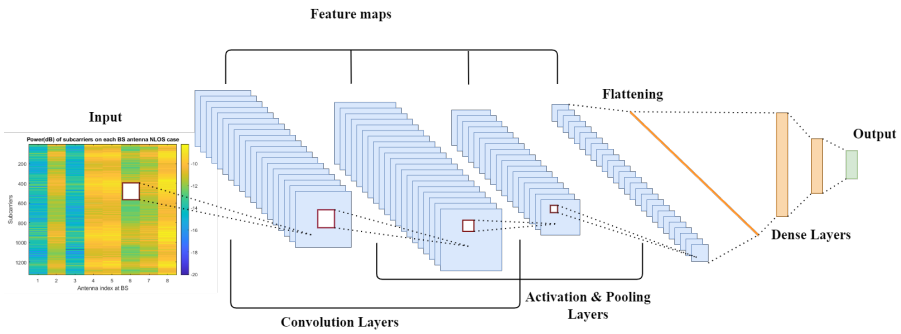

Figure 5.3: CNN architecture

Figure 5.3, shows the types of layers that are involved in a CNN architecture [22]. Before delving into the list of definitions, it is important to note that a feature map, although not a layer itself, is a crucial element in CNN. It represents the output of a convolutional layer, capturing distinctive features present in the input data or previous feature maps. The resulting feature maps undergo flattening into one-dimensional vectors. This transformation prepares them to be fed into a fully connected layer for tasks such as categorization or regression.

- **Input layer:** It is the layer in which we give input to our model. In CNNs,

generally, the input will be an image or a sequence of data. This layer holds the raw input of the data and sends it to the convolutional layer.

- **Convolutional layer:** This layer is used to extract the features from the input dataset. It applies a set of learnable filters, known as the kernels, to the input data. The filters/kernels are smaller matrices, usually 2×2, 3×3, or 5×5 -sized. It slides over the input data and computes the dot product between the kernel weights and the corresponding input data. The output of this layer is referred to as feature maps.
- **Activation layer:** By adding an activation function to the output of the preceding layer, activation layers add non-linearity to the network. It will apply an element-wise activation function to the output of the previous layer. Some common activation functions are Rectified Linear Unit (ReLU), Hyperbolic Tangent (Tanh), softmax, and Leaky ReLU, etc. In CNNs it is typical to implement activations as ReLU functions. Because activation functions operate element-wise, they are used the same way for the convolutional layers as for the linear layers. Thus, the activation layer doesn't change the dimensions of the data. ReLU is used as the activation function in this study for all of the convolutional layers. For the hidden dense layers within the CNN we have used ReLU as the activation function, but for the last dense layer, we have used softmax as the activation function. The softmax activation function constrains the output neuron values to range between zero and one, enabling them to represent probabilities within this interval.
- **Pooling layer:** This layer downsamples the data to reduce computation complexity. It is periodically inserted in the CNN and its main function is to reduce the size of the data, which makes the computation fast, reduces memory, and also prevents overfitting. Two common types of pooling layers are max pooling and average pooling, and in this study, max pooling is considered. Max pooling performs downsampling by dividing the input into non-overlapping rectangular regions and taking the maximum value from each region to form a smaller output matrix.
- **Dense layer:** It takes the input from the previous layer and computes the final classification or regression task.
- **Output layer:** The output from the fully connected layers is then fed into a logistic activation function for classification tasks like sigmoid or softmax which converts the output of each class into the probability score.

Typically, CNNs employ a cascade of L Convolutional Activation Pooling (CAP) layers. Each CAP layer is composed of a convolutional operation of its input with K convolutional Kernels, then a non-linear transformation, i.e., activation function, and next a pooling layer, respectively [14].

5.2.2.2 Motivations of having CNNs

CNNs have consistently achieved state-of-the-art performance in various domains, including image and signal processing. Applying CNNs to channel matrices can

leverage this proven capability to achieve good performance in extracting sensing information from the channel estimates. CNN architectures are commonly employed, and they are particularly suitable for handling inputs organized in grid-like structures, such as images represented as two-dimensional pixel grids.

In this study, the dataset is represented in the frequency domain, and the samples are the frequency response of the channel with complex coefficients. As we have already discussed in chapter 2 the matrix of the channel is two-dimensional with the size of $M_{\mathrm{R}} \times M_{\mathrm{T}}$, this grid-like structure is suitable for using CNN and it provides ease of implementation without transforming the samples into alternative domains e.g., delay-angle domain [14]. CNNs build a hierarchical representation of data, which can be particularly useful for channel matrices. Lower layers might capture local features like small-scale fading effects, while higher layers capture more global features like large-scale fading or overall channel gain. The nonlinear activation functions in CNNs allow them to learn complex mappings from the input channel matrices to the desired output. CNNs have shown robustness to noise in various applications. In the context of wireless communication, this means better performance in real-world conditions where the channel estimates may be noisy or distorted.

The CNN models introduced in the upcoming chapter could be enhanced in terms of computational complexity and learning efficiency by incorporating sparse interaction and parameter-sharing properties. Additionally, the BS, equipped with multiple antennas, can estimate the response at various frequency samples, allowing the channel to be represented in the delay-angle domain, an approach not yet explored, but promising for future research.

Chapter 6

Simulations and Results

In this chapter, we will examine channel models and also derive a neural network to extract obstacle features from it, for two distinct WINNER II channel scenarios, C1 and A1. It is important to note that in all subsequent case studies, we have focused on a single-channel realization for the uplink, and we have also assumed the channel to be static during the ULSRS transmission.

6.1 Dataset generation

This section outlines the procedure for deriving the frequency response from the CIR generated by the WINNER II channel model. This will be leveraged to generate a dataset for the channels estimated at the BS under the considered scenarios. By applying a Fourier transform to the time-domain CIR data, the transfer function of the simulated wireless channel is obtained. The purpose is that we have to adapt to the 5G-NR system model where we can only get estimates of the narrowband channels at each subcarrier.

Applying a Fourier transformation to the impulse response in Equation (3.1) yields the frequency-domain transfer function $\mathbf{H}(f)$ of the wireless channel. The mathematical expression of $\mathbf{H}(f)$ is expressed as follows:

$$\mathbf{H}(f) = \mathcal{F}\{\mathbf{h}(\tau)\}, \tag{6.1}$$

As 5G-NR systems employ a discrete number of narrowband subcarriers, the channel estimates available at the BS would correspond to:

$$\mathbf{H}(k) = \sum_{n=0}^{N-1} \boldsymbol{\alpha}_n \, e^{-j2\pi n f_k \tau_n}, \tag{6.2}$$

where $k = 1, \ldots, K$ is the subcarrier index, with K corresponding to the total number of subcarriers which is considered as 201 in the C1 scenario and 1332 in the A1 scenario.

6.2 C1 scenario using WINNER II channel output

The C1 scenario is simulating a suburban area. Our objective was to analyze the link conditions between a single UE and a BS using the WINNER II channel model. Specifically, we aimed to determine if the link exhibited LOS or NLOS characteristics. The ULSRS is not utilized in this part of our analysis and perfect channel estimates are assumed, i.e., without any noise.

For the simplicity of implementation, we considered an ULA comprising 64 antenna elements on the BS side, while the UE side featured a single antenna. The BS was positioned at a height of 25 meters above the ground, whereas the UE was situated at a height of 1.5 meters. The carrier frequency employed in our analysis is 3.5 GHz.

6.2.1 Result Analysis of WINNER II Channel Output

In this section, we have provided some examples of C1 scenario channel outputs. The depicted figures, namely Figures 6.1 and 6.2, provide visual representations of the channel condition observed in the C1 scenario under the influence of LOS propagation.

In Figure 6.1, the influence of LOS propagation becomes clearly noticeable as we observe a consistent disparity in signal power at the BS, with the first cluster consistently exhibiting superior strength compared to the subsequent clusters. Figure 6.2 represents the transfer function of the LOS propagation where the channel bandwidth has been divided into 201 subbands with 100 kHz frequency spacing. LOS propagation exhibits minimal delay spread because the signal travels directly from the transmitter to the receiver without significant reflections or scattering. This results in a short impulse response. The frequency response of a LOS channel is generally smooth and flat, indicating minimal frequency-selective fading compared to NLOS scenario.

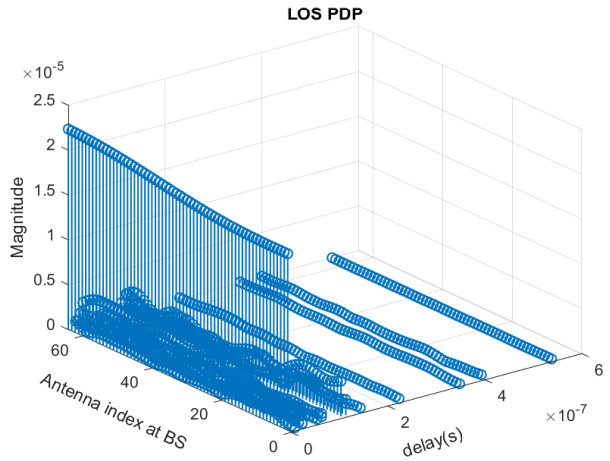

Figure 6.1: Cluster Power For C1 Scenario - LOS

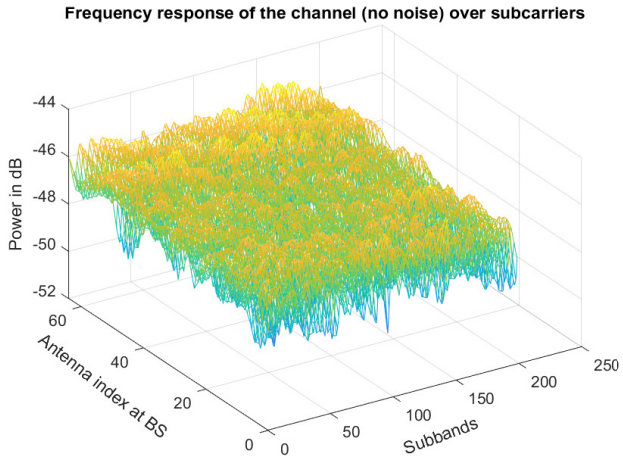

Figure 6.2: Transfer Function For C1 Scenario - LOS

Figures 6.3 and 6.4 depict the channel condition under the NLOS propagation condition. In Figure 6.3, it is observed that neither of the clusters exhibits consistently high or low power levels. This observation suggests that the channel in NLOS condition is obstructed, meaning that there are obstacles or obstructions between the UE and the BS that prevent a clear LOS connection. These obstructions can cause variations in the received power levels at the BS from different antennas and clusters, resulting in an irregular power distribution pattern. These obstacles can include buildings, trees, or other physical structures that impede the propagation of electromagnetic waves. Figure 6.4 illustrates the transfer

function for the C1 scenario under NLOS propagation conditions, with the same bandwidth and frequency spacing as the LOS case. It is evident that due to the presence of obstacles between the BS and UE, the received power at the BS exhibits significant fading dips across various subbands w.r.t the antennas at the BS.

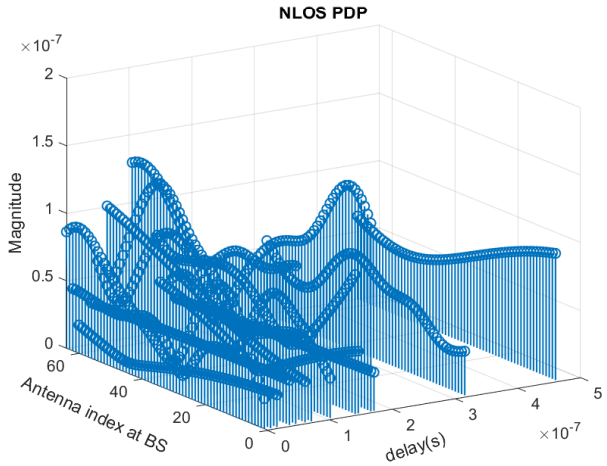

Figure 6.3: Cluster Power For C1 Scenario - NLOS

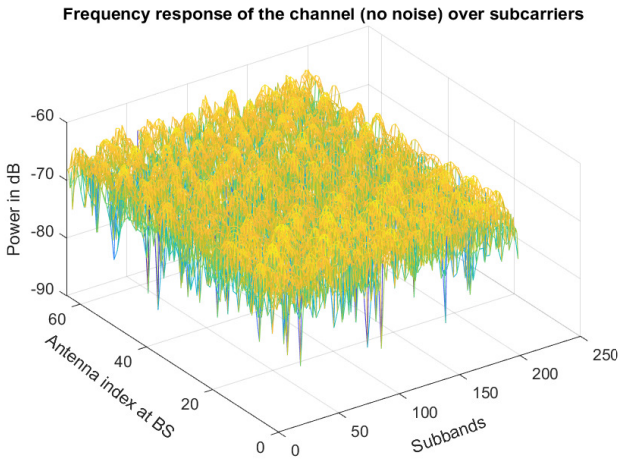

Figure 6.4: Transfer Function For C1 Scenario - NLOS

6.2.2 Deep Learning model for C1 Scenario

To accomplish our objective, it was necessary to generate a dataset large enough for training a deep learning model. This dataset was created by randomly assigning positions to the UE within the layout of the C1 scenario (1000 meters in this study), considering both LOS and NLOS conditions. This approach ensures the inclusion of diverse UE positions, thereby enabling the model to be trained independently of specific UE locations. Ultimately, we obtained a dataset consisting of 4000 samples of transfer functions representing the channel models for both LOS and NLOS scenarios. With the dataset prepared, our subsequent task involved constructing a neural network , used to generate a data-based detector of obstacles (LOS/NLOS).
The dimensions of our dataset are 4000 samples, encompassing both real and imaginary components, with 64 antenna elements on the receiving side and 201 frequency samples. To illustrate the adjustment of the dataset dimensions and the tailored architecture of the model, please refer to Figure 6.5.

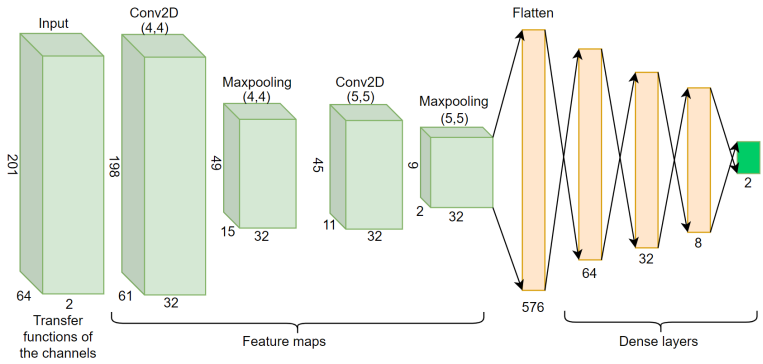

Figure 6.5: Layers in the Deep Learning Model for C1 Scenario

We used a cascade of 2 CAP layers. The first layer is a convolutional 2D with a kernel size of 4×4 and an output size of 32. ReLU is used as the activation function as mentioned within the Section 5.2.2.1. Then, a max pooling layer of size 4×4 is used to downsample the data to reduce computation complexity. Then, feature maps of the described layers are used as input to the next convolutional layer with a kernel size of 5×5, and an output size of 32, followed by a max pooling layer of size 5×5. Then, the feature maps are flattened and prepared for the dense layers. The kernel size of the first convolutional layer is smaller than the second convolutional layer, which might allow the model to capture low-level features such as small-scale fading effects and local information, whereas the second convolutional layer with a larger kernel size tends to capture more global features, including large-scale fading or overall channel gain. This model has two possible outputs, corresponding to the LOS and NLOS cases. Softmax is used as the activation function of the final dense layer, to calculate the probability score.

Layer (type)	Output Shape	Param #
Conv2D_1 (Conv2D)	(None, 198, 61, 32)	1056
max_pooling2d (MaxPooling2D)	(None, 49, 15, 32)	0
Conv2D_2 (Conv2D)	(None, 45, 11, 32)	25632
max_pooling2d_1 (MaxPooling2D)	(None, 9, 2, 32)	0
dropout (Dropout)	(None, 9, 2, 32)	0
flatten (Flatten)	(None, 576)	0
dense_3 (Dense)	(None, 64)	36928
dense_4 (Dense)	(None, 32)	2080
dropout_1 (Dropout)	(None, 32)	0
dense_5 (Dense)	(None, 8)	264
dense_6 (Dense)	(None, 2)	18

Total params: 65978 (257.73 KB)
Trainable params: 65978 (257.73 KB)
Non-trainable params: 0 (0.00 Byte)

Figure 6.6: Deep Learning Model Summary for C1 Scenario

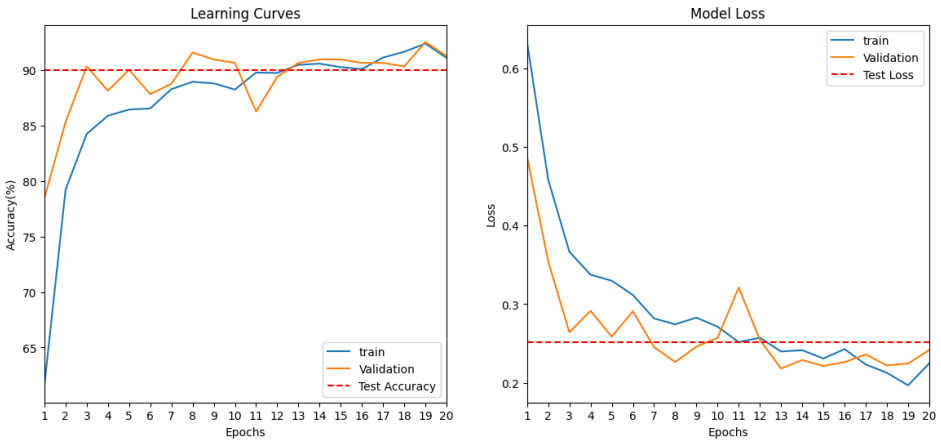

Figure 6.7: Learning Curves and Model Loss for C1 Scenario

The CNN model depicted in Figure 6.5 for C1 scenario, was trained with a batch size of 10 and 20 epochs. The learning curves are shown in Figure 6.7 with a test loss of 0.27 and test accuracy of 90%. It means the model correctly predicts the labels for a large portion of the unseen test data and based on the test loss, which indicates that the predictions are not only correct but also confident and close to

the true values.

6.3 A1 scenario using Uplink SRS

This model allows for seamless transitions between different propagation conditions, notably between LOS and NLOS scenarios, within the same WINNER II framework. Specifically, in the A1 (indoor) scenario, a transition from LOS to NLOS can occur when the UE moves from the LOS corridor, where the BS is situated, into a perpendicular corridor. Our study employed a configuration consisting of a single antenna at the UE side and 8 antenna elements arranged in a ULA structure at the BS side.

An analysis of this particular case indicates that such transitions can be adequately represented by utilizing the A1 LOS and NLOS path loss models outlined in Section 3.3.1.1. In the context of Figure 6.8, let's denote the distance along the LOS corridor (where the BS is situated) to the center of the intersection of the corridors as d_1, and the distance between the UE and the center of the intersection of the corridors as d_2. The A1 LOS path loss model is deemed suitable for values of d_2 that are smaller than $3F_1$, where F_1 corresponds to the radius of the first Fresnel zone. The ith Fresnel ellipsoid or zone is the one that results in a phase shift of $i \cdot \pi$ [2]. For values of d_2 greater than $3F_1$, the A1 NLOS path loss model can be employed. It is worth noting that, in most cases, reasonably accurate results can also be achieved by setting the transition distance equal to half the width of the LOS corridor.

In this section, we use ULSRS to detect and analyze changes in link status, enabling informed decision-making based on variations in the UE's communication channel. The following are the use cases of UE's link status detection and analysis.

1. The directional movement of the UE can be characterized by its relative motion concerning the intersection point of the corridors. This encompasses two distinct scenarios: when the UE is moving away from the intersection point and when it is moving towards it.
2. UE's arrival time to the threshold line where the link state transitions from NLOS to LOS as shown in Figure 6.8. By estimating the approximate arrival time of the UE at the threshold line, the BS gains the ability to proactively plan scheduling and allocate resources accordingly. This facilitates effective resource management and optimization in wireless communication systems. For this use case, we have assumed positioning capabilities at the BS.
3. Continuing our investigation, we aim to approximately determine the size of the obstacle that impedes the LOS, enabling effective strategies to optimize wireless communication performance in obstructed environments.

In the A1 scenario, a choice can be made between two distinct wall materials, each characterized by unique path losses classified as CR-heavy and CR-light. It

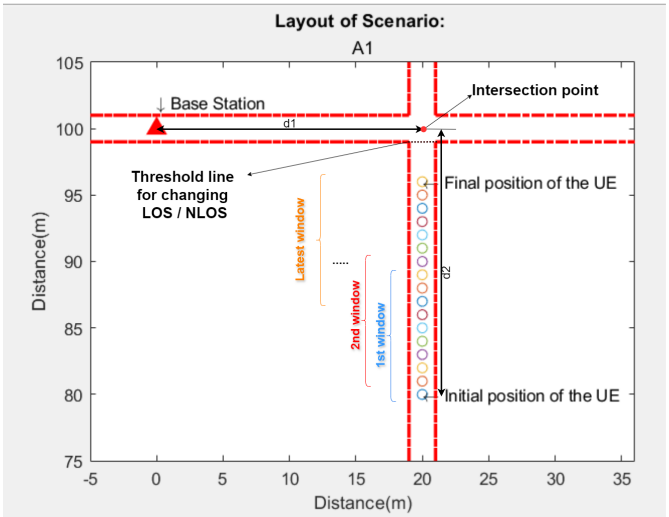

Figure 6.8: SRS window size of 10

is important to note that the consideration of PL for the wall is applicable solely in NLOS conditions, as there are no obstructions (i.e., walls) between the UE and the BS in LOS conditions. The BS and the UE are positioned at heights of 2.5 meters and 1.5 meters above the ground, respectively. The corridor width is set at 2 meters, and the carrier frequency utilized for communication is 3.5 GHz.

6.3.1 Detecting the UE Movement direction

By employing a window of 10 ULSRS transmissions we can effectively monitor changes in the uplink channel. We can ascertain whether the UE is moving towards or away from the intersection point. As illustrated in Figure 6.8, when the UE is located in a corridor perpendicular to the one where the BS is positioned, the link state is classified as NLOS, and the UE traverses a distance denoted as d_2. In this particular scenario, two situations can arise: the UE is moving away from the intersection point or approaching it. Furthermore, due to the presence of different wall materials between the BS and the UE, two distinct path loss conditions emerge, referred to as CR light and CR heavy. Consequently, four distinct outcomes can be identified, each representing a unique combination of the UE's movement direction and the prevailing path loss condition.

1. UE is moving **towards** the intersection point with **heavy** walls
2. UE is moving **away** from the intersection point with **heavy** walls
3. UE is moving **towards** the intersection point with **light** walls
4. UE is moving **away** from the intersection point with **light** walls

In this part of the section, two examples of four possible outcomes will be studied in more detail.

To determine the movement direction of the UE along d_2, we need to perform multiple ULSRS transmissions, each within the size of the SRS window. The direction is then inferred from the estimated channels derived from the received ULSRS signals from the UE.

Figure 6.9 provides an illustrative example within the context where the UE moves towards the intersection point along the corridor denoted as d_2, while heavy walls separate the BS and the UE, and Figure 6.10 provides an example where the UE moves away from the intersection point along the d_2 corridor, while light walls separate the BS and the UE. The SRS window size is defined as 10 ULSRS, as previously discussed. The frequency response of the channel is computed for each subcarrier within every ULSRS, indicated by the presence of red lines demarcating each ULSRS interval. Notably, the scenario encompasses a distance (d_1) of 20 meters between the BS and the intersection point, with a corridor width of 2 meters.

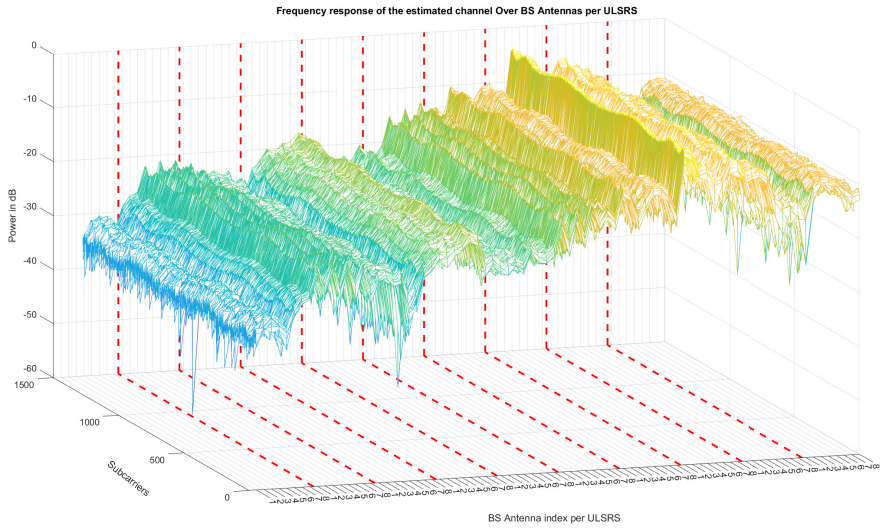

Figure 6.9: Channel Estimations for Received ULSRS Signals within SRS Window at BS with heavy walls, UE is moving towards the intersection point

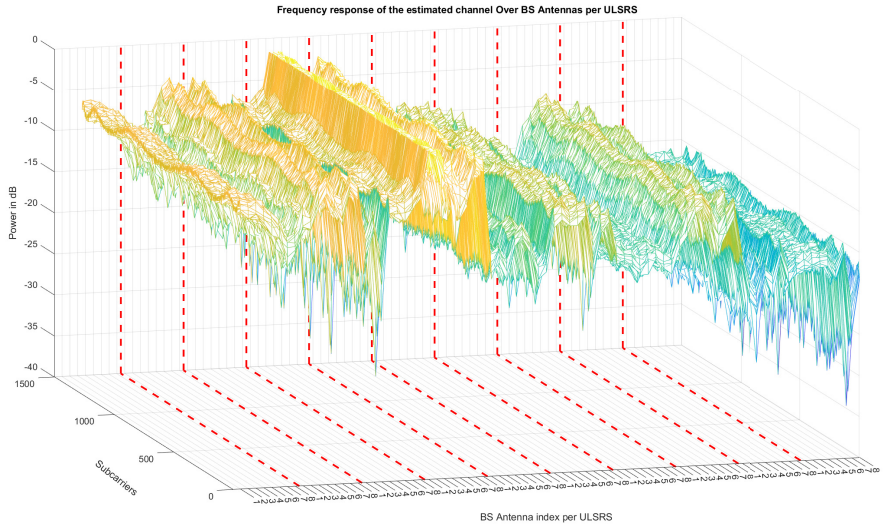

Figure 6.10: Channel Estimations for Received ULSRS Signals within SRS Window at BS with light walls, UE is moving away from intersection point

Figure 6.11 depicts one realization of CIR that is related to the UE at the initial position of the movement (d_2), 40 meters away from the intersection point, and the distance between the BS and the intersection point (d_1) is 20 meters. The corridor width is 2 meters in this example and heavy walls are present between the BS and the UE. Further details regarding the configuration of this section are presented in Table 6.1.

Parameter	Value
Corridor Width	2 m
SRS window size	10
Carrier freq	3.5GHz
Bandwidth	20MHz
Number of PRBs	111
Number of subcarriers	1332

Table 6.1: Configurations used in Figures: 6.11 and 6.12

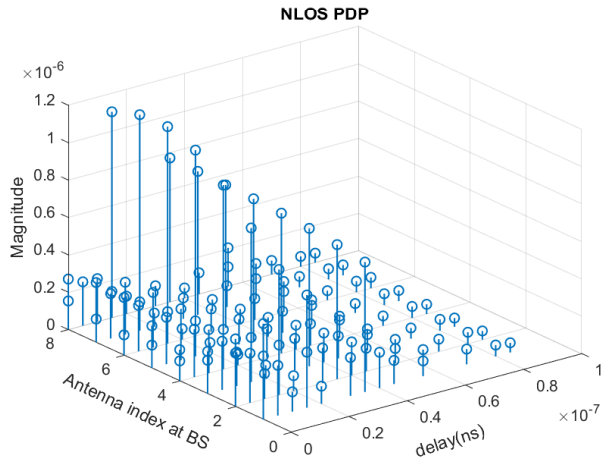

Figure 6.11: PDP of the channel impulse response for NLOS case

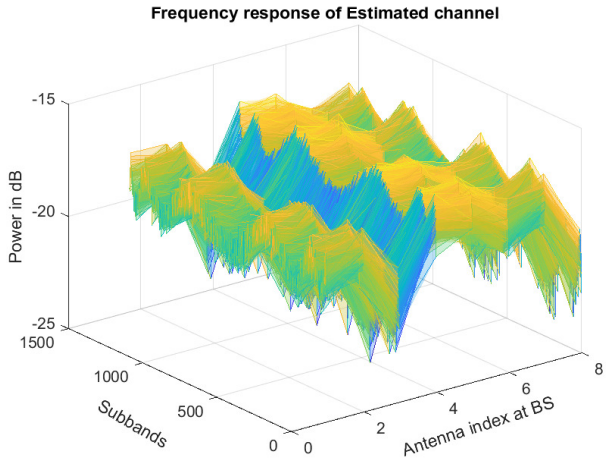

Figure 6.12: Transfer Function For A1 Scenario - NLOS

Figure 6.11 provides valuable insights into the characteristics and behavior of the channel in the examined scenario, shedding light on the power distribution and variations in received power for the NLOS case within the A1 scenario. Figure 6.12 shows the frequency response of the channel when the UE is at the initial position of the movement, i.e. 40 meters away from the intersection point.

6.3.1.1 Deep learning model for UE movement direction along d_2

The input to the CNN comprises a window of ULSRS signals with a size of 10, aiming to detect both the UE movement direction along d_2 and the type of wall between the UE and the BS. The input data is structured with dimensions of 20 by 1332 by 8. Here, the first dimension (20) represents the number of ULSRS signals within the window size of 10 by 2, considering both the real and imaginary parts of the signals separately. The second dimension (1332) corresponds to the number of subcarriers (111 PRBs$\times$12 subcarriers), and the third dimension, with a size of 8, indicates the number of antenna elements deployed at the BS side, while the UE is equipped with a single antenna. The layers used in this model are described in Figure 6.13.

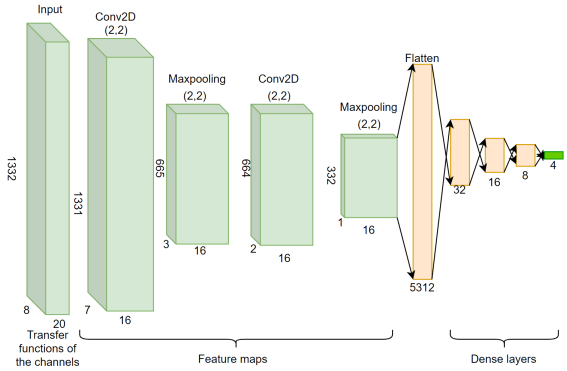

Figure 6.13: Layers in the Deep Learning Model to detect the UE's movement direction and wall material

The first layer is a 2D convolutional layer with a 2×2 kernel and an output size of 16. ReLU is used as the activation function as it is mentioned within Section 5.2.2.1. Subsequently, a max pooling layer with a size of 2×2 is applied to downsample the data, thereby reducing computational complexity. The feature maps from the previous layers are then fed into the next convolutional layer, which has a 2×2 kernel and an output size of 16. This is followed by a max pooling layer with a 2×2 size. The convolutional layers extract the features of the input dataset, including the channel gain, small-scale fading, and large-scale fading characteristics of the samples within the dataset. Subsequently, the feature maps are flattened and prepared for the dense layers. At the final dense layer, we have four different outputs in this model, considering all possible classifications discussed. The activation function used in this layer is softmax.

Layer (type)	Output Shape	Param #
Conv2D_1 (Conv2D)	(None, 1331, 7, 16)	1296
max_pooling2d (MaxPooling2D)	(None, 665, 3, 16)	0
Conv2D_2 (Conv2D)	(None, 664, 2, 16)	1040
max_pooling2d_1 (MaxPooling2D)	(None, 332, 1, 16)	0
dropout (Dropout)	(None, 332, 1, 16)	0
flatten (Flatten)	(None, 5312)	0
dense_3 (Dense)	(None, 32)	170016
dense_4 (Dense)	(None, 16)	528
dropout_1 (Dropout)	(None, 16)	0
dense_5 (Dense)	(None, 8)	136
dense_6 (Dense)	(None, 4)	36

Total params: 173052 (675.98 KB)
Trainable params: 173052 (675.98 KB)
Non-trainable params: 0 (0.00 Byte)

Figure 6.14: Deep Learning Model Summary to detect the UE's movement direction and wall material

The dataset for this model contains 4000 SRS windows, and each SRS window consists of 10 estimated frequency responses over subcarriers of the OFDM-based system. Thus, throughout the dataset generation process, a total number of 40,000 channel realizations are generated. The dataset consists of the channel estimates at each OFDM subcarrier and BS antenna, that are obtained from the received ULSRS on the BS side.

Figure 6.15 depicts the case where the UE is positioned 40 meters away from the intersection point. In this sample, only one ULSRS is transmitted from the UE to the BS. Both cases share the same environmental conditions, with the only difference being the material of the wall, impacting the PL exclusively. As mentioned before, the wall materials can be either heavy or light walls, and the PL calculations are dependent on the wall material and the number of walls that are situated between the UE and the BS. In the case that there is a heavy wall in between the BS and the UE, the signal strength is more attenuated than in the case where there is a light wall in between the BS and the UE. So, the model will detect these differences, and it is trained to detect the signal strength change trends to distinguish the wall material, i.e. heavy and light walls (see Section 3.3.1)

The CNN model is depicted in Figure 6.13 for UE movement direction and wall material detection. The model was trained with a batch size of 10 and 15 epochs. The learning curves are shown in Figure 6.16 with a test loss of 0.13 and test accuracy of 95%.

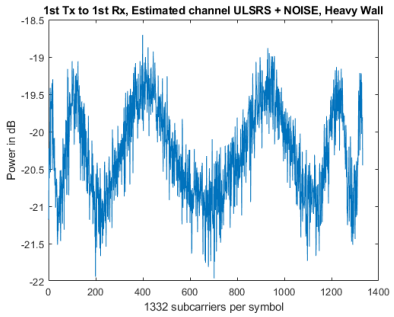

(a) Estimated channel with Heavy wall between the UE and the BS

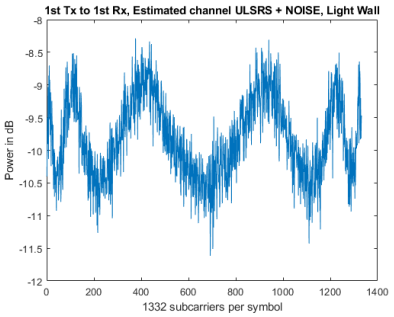

(b) Estimated channel with Light wall between the UE and the BS

Figure 6.15: Path-loss Comparison of Light and Heavy Walls

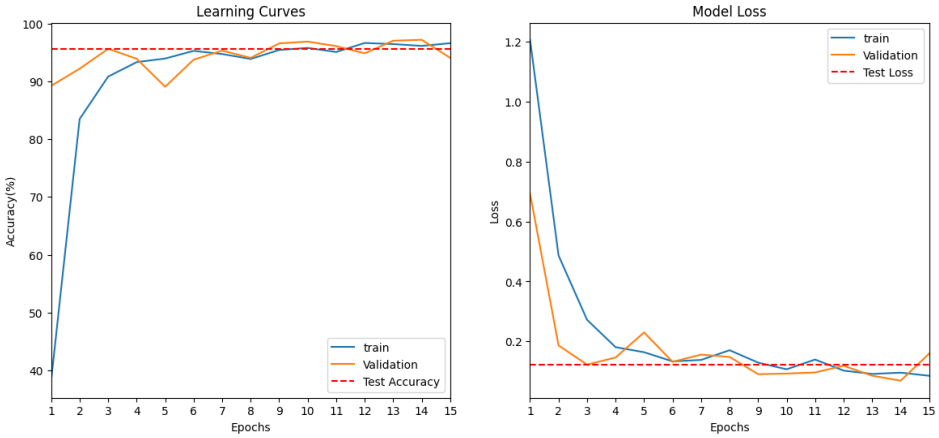

Figure 6.16: Learning Curves and Model Loss to detect the UE's movement direction and wall material

6.3.2 UE approximate arrival time at the threshold line

In this part, one use case of the CNN model that we discussed in Section 6.3.1.1 is explained with an example. It is assumed that the BS possesses positioning capabilities and has access to precise UE location information. Leveraging precise knowledge of the UE's location and the periodicity of the SRS signal, we can estimate the approximate arrival time of the UE at the threshold line shown in Figure 6.8 at which the link state transitions from NLOS to LOS. The speed of the UE, in conjunction with the SRS periodicity, plays a crucial role in this regard, as higher UE speeds necessitate shorter SRS intervals. To track the UE's positions more accurately, it is possible to increase the window size, e.g., employing a window of 50 ULSRS. The decision to adjust the window size depends on the specific scenario. It is worth mentioning that, it is also not desirable to have too high SRS

Parameter	Value
SRS periodicity	5 ms
d_2 at initial UE position	40 m
d_2 at current UE position	15 m
Corridor width	2 m
Number of received ULSRS	2500

Table 6.2: System configurations of example 6.1

periodicity or window size since that would mean that we reduce the resources employed for communication purposes, so we have to find a good compromise between sensing performance and communication performance. For instance, if the UE is situated in a high-speed train, employing shorter SRS intervals and a larger window in the time domain could enhance the accuracy of movement direction and position tracking. Initially, the BS receives the first ULSRS and buffers it. Once the number of buffered ULSRS reaches the SRS window size, which is 10 ULSRS in this case, the BS utilizes this batch as input for the deep-learning model. Subsequently, it awaits the arrival of the second batch. Using these received batches, each consisting of 10 ULSRS, the BS determines the UE's direction along d_2. If the UE is approaching the intersection point, the time of arrival at the threshold line can be calculated. However, if the UE is moving away from the intersection point, no further processing occurs. By leveraging the periodicity of the SRS and the distance covered by the UE within the SRS intervals, the average speed of the UE can be determined, utilizing the location data obtained from the positioning features available at the BS. An instance of such positioning features is the Positioning Reference Signal (PRS) employed in the 3GPP 5GNR specifications. However, an in-depth discussion on positioning features falls beyond the scope of this thesis.
Given that the BS is aware of the threshold line shown in Figure 6.8 at which the link state transitions from NLOS to LOS, it is possible to compute an estimated arrival time for the UE at the threshold line using the following equations:

$$V_{avg} = \frac{X_{traveled}}{T_{ULSRS} \cdot N_{ULSRS}}, \tag{6.3}$$

where V_{avg} is the UE's average speed, $X_{traveled}$ is the distance traveled by the UE from the initial position to the current position of the UE, T_{ULSRS} is the SRS periodicity and N_{ULSRS} is the number of ULSRS received by the BS during the observation time.

$$t_{LOS} = \frac{x_{LOS}}{V_{avg}}, \tag{6.4}$$

where t_{LOS} is the UE arrival time to the threshold line, x_{LOS} is the UE distance to the threshold line.

Example 6.1: Here, is an example of the arrival time to the threshold line. Assume a network with the configurations according to Table 6.2.

The average speed of the UE is:

$$\mathrm{V_{avg}} = \frac{40 - 15}{5 \cdot 10^{-3} \cdot 2500} = 2\ \mathrm{m/s}. \tag{6.5}$$

Assume that the average speed of the UE will be constant and that the direction of the movement will not be changed for the rest of the path to the intersection point. In this example, as the corridor width is 2 meters, the threshold line, i.e., where the distance between the UE and the intersection point, is 1 meter, which is half of the corridor width. The arrival time of the UE to the threshold line is:

$$\mathrm{t_{LOS}} = \frac{\text{15-1}}{2} = 7\ \mathrm{s}. \tag{6.6}$$

6.3.3 Size of the obstacle that has blocked the LOS

In this subsection the assumptions considered in Section 6.3.2 are valid. Assume that the UE is situated within the LOS region and moves on a straight line perpendicular to the corridor where the BS is positioned. Also, the UE maintains a constant average speed (V_{avg}) and the SRS periodicity (T_{ULSRS}) is assumed to be known. It becomes viable to determine the amount of time it takes the UE to transition from LOS to NLOS and back to LOS again. Consequently, leveraging the T_{ULSRS}, the V_{avg}, and the distance traveled by the UE i.e, the number of ULSRSs which are received by the BS during the NLOS link state ($N_{\mathrm{ULSRS,NLOS}}$) , it becomes feasible to approximate the size of the obstacle (L_{obstacle}) shown in Equation (6.7), responsible for temporarily disrupting the LOS path. For this purpose, we have generated a dataset of random locations within the LOS area of the A1 scenario, with a corridor width of 2 meters, and then trained a deep learning model that detects the LOS and NLOS link state of the UE. It is worth noting that, in this context, it is assumed that the distance between the UE and the obstacle is assumed to be extremely close to zero, thus resulting in no diffraction of the signal, which occurs when electromagnetic waves encounter an obstacle, causing them to spread out or bend around it.

$$L_{\mathrm{obstacle}} = N_{\mathrm{ULSRS,NLOS}} \cdot T_{\mathrm{ULSRS}} \cdot V_{\mathrm{avg}} \tag{6.7}$$

6.3.3.1 Deep learning model for LOS/NLOS detection

For this segment of the research, the aim is to build a model to detect the link state of the UE, whether it is LOS or NLOS, and use the model for computing the size of the obstacle that has blocked the LOS within the LOS area in the A1 scenario. A dataset comprising 4000 samples for LOS and NLOS scenarios is employed. Each sample encompasses the estimates of the channel across the subcarriers of the OFDM-based system.

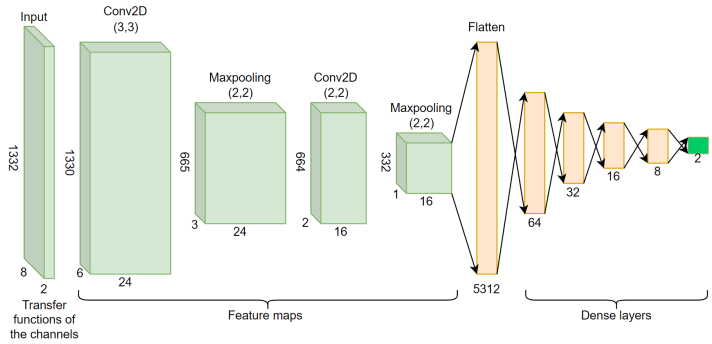

Figure 6.17: Layers in the Deep Learning Model for A1 scenario to detect the obstacle

Layer (type)	Output Shape	Param #
Conv2D_1 (Conv2D)	(None, 1330, 6, 24)	456
max_pooling2d (MaxPooling2D)	(None, 665, 3, 24)	0
Conv2D_2 (Conv2D)	(None, 664, 2, 16)	1552
max_pooling2d_1 (MaxPooling2D)	(None, 332, 1, 16)	0
dropout (Dropout)	(None, 332, 1, 16)	0
flatten (Flatten)	(None, 5312)	0
dense_2 (Dense)	(None, 64)	340032
dropout_1 (Dropout)	(None, 64)	0
dense_3 (Dense)	(None, 32)	2080
dense_4 (Dense)	(None, 16)	528
dropout_2 (Dropout)	(None, 16)	0
dense_5 (Dense)	(None, 8)	136
dense_6 (Dense)	(None, 2)	18

Total params: 344802 (1.32 MB)
Trainable params: 344802 (1.32 MB)
Non-trainable params: 0 (0.00 Byte)

Figure 6.18: Deep Learning Model Summary to detect obstacle

Figures 6.17 and 6.18 shows, a detailed understanding of the CNN model implementation to determine the L_{obstacle}. The initial layer is a 2D convolutional layer with a 3×3 kernel and an output size of 24. ReLU is employed as the activation function, as noted in Section 5.2.2.1. Next, a max pooling layer with a size of 2×2 is applied to downsample the data, thus reducing computational complexity. The feature maps from the preceding layers are then directed into the subsequent convolutional layer, which employs a 2×2 kernel and yields an output size of 16. Subsequently, a max pooling layer with a 2×2 size is applied. The convolutional layers extract various features from the input dataset, encompassing characteris-

tics such as channel gain, small-scale fading, and large-scale fading of the samples within the dataset. Following this, the feature maps are flattened and readied for the dense layers. The possible outputs of this model are LOS and NLOS as we discussed and the softmax activation function is used for the final dense layer to calculate the probability of the possible classifications.

The CNN model shown in Figure 6.17 was trained using a batch size of 10 and 15 epochs. The learning curves shown in Figure 6.19 demonstrate the model's performance during the training process. Notably, the model achieved a test loss of 0.24, and a test accuracy of 92%.

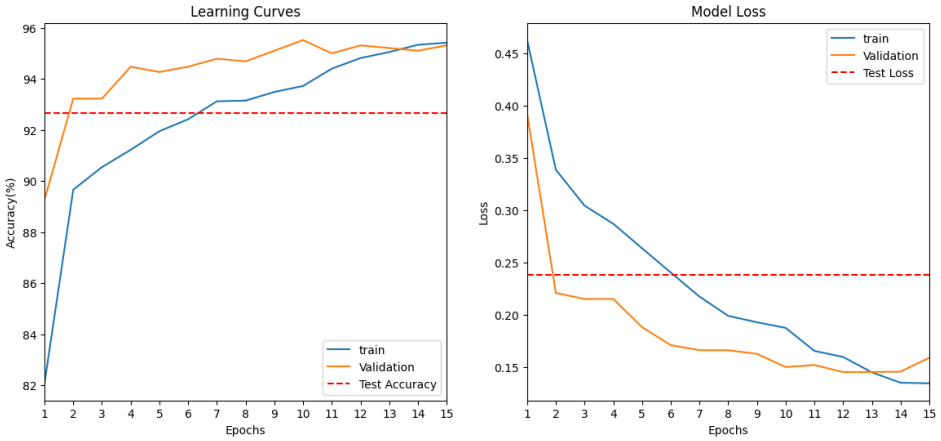

Figure 6.19: Learning curves and Model Loss to detect the obstacle in LOS region

Example 6.2: Here is an example of this use case to calculate the size of the obstacle that has blocked the LOS. Assume a network with the configurations according to Table 6.3. Consider the UE is moving on a straight line in a northern direction at a constant average speed and transmitting ULSRS signals every 5 ms as shown in Figure 6.20. It passes behind an obstacle, causing LOS to be obstructed, then the UE continues its journey until it clears the obstacle, and the link status returns to LOS. By calculating the duration of time when the link status is NLOS, it is possible to calculate the size of the obstacle. The trained model is used to detect the LOS / NLOS condition of the UE's link.

In this example, the number of ULSRS that are received in NLOS link state based on the deep-learning model output which gives $N_{ULSRS,NLOS} = 58$. Substituting this value along with the T_{ULSRS} and V_{avg} from Table 6.3 in Equation (6.7), then the approximate size of the obstacle ($L_{obstacle}$) is:

$$L_{obstacle} = 58 \cdot 5 \cdot 10^{-3} \cdot 2 = 58 \text{ cm}. \tag{6.8}$$

Notably, Equation (6.8) shows, the CNN model's estimated obstacle size is very close to the actual size i.e, 60cm, demonstrating high accuracy. This suggests, the CNNs effectively captures relevant visual cues even in complex environments.

Parameter	Value
T_{ULSRS}	5 ms
Actual size of the obstacle	60 cm
Number of received ULSRS	160
V_{avg}	2 m/s
d_1	10 m

Table 6.3: System configurations of example 6.2

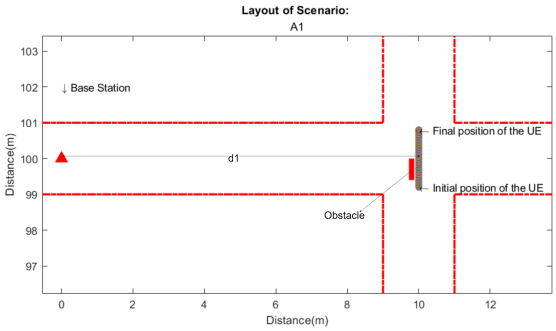

Figure 6.20: Layout of the example 6.2

Based on the findings presented in Figure 6.21, it is clear that, when there is an obstacle between the BS and UE, the signal experiences a much greater decrease in strength compared to the areas without any obstructions. This trivial observation can be significantly helpful for extracting interesting sensing information from the available channel estimates, that has been showcased throughout this work.

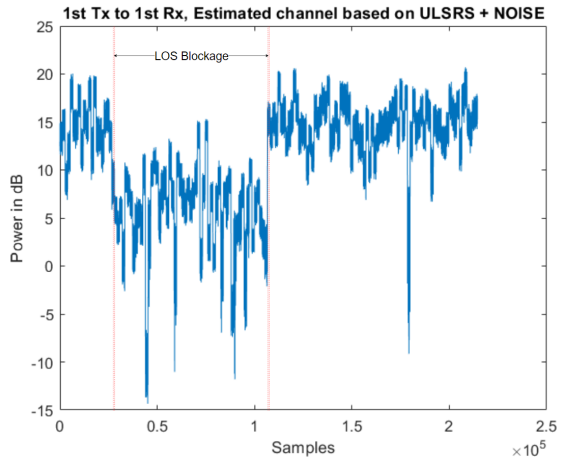

Figure 6.21: Frequency response of the channel of 160 received ULSRS

Chapter 7

Conclusions & Future work

7.1 Conclusions

This study investigates UE-BS link characteristics in A1 and C1 scenarios using the WINNER II channel model. The focus is to extract sensing features from the channel estimates under LOS and NLOS conditions.

In the outdoor C1 scenario, we focused on LOS and NLOS detection using the WINNER II channel model. LOS propagation in the C1 scenario, was characterized by distinct power disparities between the clusters, with the first cluster consistently stronger than the rest. NLOS propagation in the C1 scenario exhibited irregular power levels across clusters, indicating obstructed channels due to physical obstacles. Specific path delays showed variations in received power, on a few clusters. Power disparities among BS antennas were observed, with constructive and destructive interference affecting reception.

To train a deep learning model for LOS/NLOS detection in the C1 scenario, a large dataset was generated, including diverse UE positions in both propagation scenarios. A neural network was designed and achieved 90% accuracy in link state detection. The study's approach ensured an appropriate dataset, and an effective architecture, for accurate link state detection. The findings provide tools for optimizing system performance in suburban outdoor communication environments.

In the A1 scenario, which simulates an indoor environment, our study investigated the link state transitions between LOS and NLOS propagation conditions. The transition distance (threshold) from NLOS-to-LOS is set equal to half the width of the LOS corridor. Channel estimations based on the pilot signals (ULSRS) enabled the detection and analysis of link status changes.

The choice of wall material (heavy or light) influences the NLOS path losses in the A1 scenario. ULSRS periodicity and window size concepts are discussed, offering means to regulate UE's uplink channel measurements. The study presents four possible outcomes based on the UE's movement direction and prevailing

path loss conditions in the A1 scenario. Deep learning techniques, specifically CNNs, are employed to detect movement direction, and classify the type of wall between the UE and the BS. The CNN model processes a window of ULSRS signals as input, achieving a 95% accuracy after training on a dataset of channel estimations. In summary, the study provides valuable insights into the A1 scenario in the WINNER II channel model, covering LOS/NLOS transitions, path loss models, ULSRS-based detection of link status changes, and the application of deep learning for movement direction detection, and wall material classification.

Furthermore, we investigated the approximate arrival time of the UE to the threshold line where the link state transitions from NLOS to LOS in the A1 scenario. This allows for proactive resource allocation and scheduling based on the estimated arrival time of the UE at the threshold line. The study assumes that the BS has positioning capabilities and access to accurate UE location information. By utilizing deep learning models to detect the UE's movement direction and leveraging the periodicity of the SRS, the average speed of the UE can be determined. Based on this information and the known threshold line, an estimated arrival time of the UE at the threshold line can be calculated.

Finally, the study proposes a deep learning model for detecting the LOS and NLOS link states in the A1 scenario with an obstacle in the LOS area, allowing for the estimation of the size of the obstacle. The model achieves 92% average accuracy in determining the link state of the UE. In summary, it presents methodologies for determining the size of the obstacle using the output of the deep learning model in the A1 scenario.

7.2 Future work

The thesis work we presented can be extended in many directions. Here, we list some future work that can be done:

- The findings of the thesis can be validated and tested in real-world scenarios to assess their applicability and performance. Field trials and measurements can be conducted to verify the accuracy of the proposed models and algorithms in different environments.
- The research can be extended to investigate the integration of the proposed techniques with other advanced wireless communication architectures. For example, the techniques could be evaluated in the context of mmWave communications, which utilize high-frequency bands above 30 GHz to achieve extremely high data rates. Assessing the performance of the techniques in these challenging and dynamic environments would further validate their effectiveness and applicability.
- Investigating the robustness of the proposed models and algorithms to changing environmental conditions, such as varying obstacle configurations, different types of walls, and dynamic mobility patterns, can be a

valuable area of research. It is important to ensure that the techniques remain effective and reliable in real-world scenarios with varying conditions.

- Further exploration can be done on the integration of the proposed techniques with positioning systems, such as GPS or indoor positioning technologies. This can enable more accurate localization of UEs and enhance the overall performance of the wireless communication system.
- Deep learning models that are trained within the scope of the thesis, could be very much improved, e.g., by translating the representation of the input data to the delay-angle domain.
- Considering the prevalent use of 30 kHz SCS in mid-band spectrum, it would be valuable to assess the feasibility and potential benefits of adopting this SCS in the proposed techniques, facilitating smoother integration with industry standards.

References

[1] A. Paulraj, "Introduction to space-time wireless communications," 2003.

[2] A. Molisch, *Wireless Communications*. IEEE Press, Wiley, 2010.

[3] P. Kyösti, J. Meinilä, L. Hentila, X. Zhao, T. Jämsä, C. Schneider, M. Narandzi'c, M. Milojevi'c, A. Hong, J. Ylitalo, V.-M. Holappa, M. Alatossava, R. Bultitude, Y. Jong, and T. Rautiainen, "Ist-4-027756 winner ii d1.1.2 v1.2 winner ii channel models," *Inf. Soc. Technol*, vol. 11, 02 2008.

[4] A. Grami, "Chapter 11 - communication networks," in *Introduction to Digital Communications* (A. Grami, ed.), pp. 457–491, Boston: Academic Press, 2016.

[5] E.-K. Hong, J.-Y. Baek, and G. Kaddoum, "A study on channel estimation algorithm with sounding reference signal for tdd downlink scheduling," in *2017 IEEE 28th Annual International Symposium on Personal, Indoor, and Mobile Radio Communications (PIMRC)*, pp. 1–6, 2017.

[6] K.-y. Lee, Y.-J. Song, and J.-S. Jang, "Adaptive downlink beamforming based on srs for channel estimation using coherence bandwidth characteristic in sub-6ghz 5g nr," in *2021 Wireless Telecommunications Symposium (WTS)*, pp. 1–5, 2021.

[7] E. Dahlman, S. Parkvall, and J. Sköld, "Chapter 8 - channel sounding," in *5G NR: the Next Generation Wireless Access Technology* (E. Dahlman, S. Parkvall, and J. Sköld, eds.), pp. 133–152, Academic Press, 2018.

[8] D. C. Moreira, L. R. Costa, Y. C. B. Silva, and I. M. Guerreiro, "Interference mitigation for dynamic tdd networks employing sounding signals," *Journal of Communication and Information Systems*, vol. 35, p. 320–332, Dec. 2020.

[9] K. Liu, S. Cai, X. Gao, X. Liu, C. Dong, Z. Zhang, J. Lian, J. Tan, L. Zhang, M. Zhang, Z. Shen, and S. Wang, "Nr enhancements for downlink mimo in rel-18," *IEEE Communications Standards Magazine*, vol. 7, no. 2, pp. 48–55, 2023.

[10] Y. LeCun, Y. Bengio, and G. E. Hinton, "Deep learning," 2015.

[11] A. Bhardwaj, W. Di, and J. Wei, *Deep Learning Essentials: Your hands-on guide to the fundamentals of deep learning and neural network modeling*. Packt Publishing Ltd, 2018.

[12] R. Rawat, J. K. Patel, and M. T. Manry, "Minimizing validation error with respect to network size and number of training epochs," in *The 2013 International Joint Conference on Neural Networks (IJCNN)*, pp. 1–7, 2013.

[13] A. Mao, M. Mohri, and Y. Zhong, "Cross-entropy loss functions: Theoretical analysis and applications," in *Proceedings of the 40th International Conference on Machine Learning* (A. Krause, E. Brunskill, K. Cho, B. Engelhardt, S. Sabato, and J. Scarlett, eds.), vol. 202 of *Proceedings of Machine Learning Research*, pp. 23803–23828, PMLR, 23–29 Jul 2023.

[14] J. Vieira, E. Leitinger, M. Sarajlic, X. Li, and F. Tufvesson, "Deep convolutional neural networks for massive mimo fingerprint-based positioning," in *2017 IEEE 28th Annual International Symposium on Personal, Indoor, and Mobile Radio Communications (PIMRC)*, pp. 1–6, 2017.

[15] I. Bilbao and J. Bilbao, "Overfitting problem and the over-training in the era of data: Particularly for artificial neural networks," in *2017 Eighth International Conference on Intelligent Computing and Information Systems (ICICIS)*, pp. 173–177, 2017.

[16] A. Wong, M. J. Shafiee, and M. St. Jules, "Micronnet: A highly compact deep convolutional neural network architecture for real-time embedded traffic sign classification," *IEEE Access*, vol. 6, pp. 59803–59810, 2018.

[17] P. Swietojanski, A. Ghoshal, and S. Renals, "Convolutional neural networks for distant speech recognition," *IEEE Signal Processing Letters*, vol. 21, no. 9, pp. 1120–1124, 2014.

[18] G. Aoki and Y. Sakakibara, "Convolutional neural networks for classification of alignments of non-coding RNA sequences," *Bioinformatics*, vol. 34, pp. i237–i244, 06 2018.

[19] D. G. Bailey, *Design for embedded image processing on FPGAs*. John Wiley & Sons, 2023.

[20] M. Valueva, N. Nagornov, P. Lyakhov, G. Valuev, and N. Chervyakov, "Application of the residue number system to reduce hardware costs of the convolutional neural network implementation," *Mathematics and Computers in Simulation*, vol. 177, pp. 232–243, 2020.

[21] K. O'shea and R. Nash, "An introduction to convolutional neural networks," *arXiv preprint arXiv:1511.08458*, 2015.

[22] M. Deprez and E. C. Robinson, "Chapter 11 - convolutional neural networks," in *Machine Learning for Biomedical Applications* (M. Deprez and E. C. Robinson, eds.), pp. 233–270, Academic Press, 2024.

Printed by Tryckeriet i E-huset, Lund 2024

LUND
UNIVERSITY

Series of Master's theses
Department of Electrical and Information Technology
LU/LTH-EIT 2024-981
http://www.eit.lth.se